On the nature of infrared-faint radio sources in the Subaru X-ray Deep and Very Large Array-VIMOS VLT Deep Survey fields

Veeresh Singh, Yogesh Wadadekar, C. H. Ishwara-Chandra, Sandeep Sirothia, Jonathan Sievers, Alexandre Beelen, Alain Omont

HAL Id: insu-03744564
https://insu.hal.science/insu-03744564

Submitted on 3 Aug 2022

On the nature of infrared-faint radio sources in the Subaru X-ray Deep and Very Large Array–VIMOS VLT Deep Survey fields

Veeresh Singh,[1,2]★ Yogesh Wadadekar,[3]★ C. H. Ishwara-Chandra,[3]★
Sandeep Sirothia,[3,4,5] Jonathan Sievers,[2] Alexandre Beelen[6] and Alain Omont[7]

[1]*Astronomy and Astrophysics Division, Physical Research Laboratory, Ahmedabad 380009, India*
[2]*Astrophysics and Cosmology Research Unit, School of Chemistry and Physics, University of KwaZulu-Natal, Durban 4041, South Africa*
[3]*National Centre for Radio Astrophysics, TIFR, Post Bag 3, Ganeshkhind, Pune 411007, India*
[4]*Square Kilometre Array South Africa, 3rd Floor, The Park, Park Road, 7405, Pinelands, South Africa*
[5]*Department of Physics and Electronics, Rhodes University, PO Box 94, Grahamstown 6140, South Africa*
[6]*Institut d'Astrophysique Spatiale, Bât. 121, Université Paris-Sud, 91405 Orsay Cedex, France*
[7]*CNRS, UMR 7095, Institut d'Astrophysique de Paris, 75014, Paris, France*

ABSTRACT

Infrared-faint radio sources (IFRSs) are an unusual class of objects that are relatively bright at radio wavelengths but have faint or undetected infrared counterparts, even in deep surveys. We identify and investigate the nature of IFRSs using deep radio ($S_{1.4\,GHz} \sim 100$ μJy beam^{-1} at 5σ), optical ($m_r \sim 26$–27.7 at 5σ) and near-infrared ($S_{3.6\,\mu m} \sim 1.3$–2.0 μJy beam^{-1} at 5σ) data that are available in two deep fields: the Subaru X-ray Deep Field (SXDF) and the Very Large Array–VIMOS VLT Deep Survey (VLA–VVDS) field. In 1.8 deg^2 of the two fields, we identify a total of nine confirmed and ten candidate IFRSs. We find that our IFRSs are high-redshift radio-loud active galactic nuclei, with 12/19 sources having redshift estimates in the range of $z \sim 1.7$–4.3, while a limit of $z \geq 2.0$ is placed on the remaining seven sources. Notably, for the first time, our study finds IFRSs with measured redshift >3.0, and also redshift estimates for IFRSs in the faintest 3.6-μm flux regime (i.e. $S_{3.6\,\mu m} < 1.3$ μJy). Radio observations show that our IFRSs exhibit both compact unresolved and extended double-lobe morphologies, and have predominantly steep radio spectra between 1.4 GHz and 325 MHz. The non-detection of all but one IFRSs in the X-ray band and the optical-to-mid-infrared colour (m_r–$m_{24\,\mu m}$) suggest that a significant fraction of IFRSs are likely to be hosted in dusty obscured galaxies.

Key words: galaxies: active – galaxies: high-redshift – infrared: galaxies – radio continuum: galaxies.

1 INTRODUCTION

In recent years, systematic searches for the optical and infrared counterparts of radio sources in deep fields have yielded a new class of radio sources called infrared-faint radio sources (IFRSs). As the name suggests, IFRSs constitute radio sources with faint or undetected near-infrared (NIR) counterparts (Norris et al. 2006, 2011b; Herzog et al. 2014). These sources were first discovered by Norris et al. (2006), who reported 22 radio sources in 3.7 deg^2 of the 1.4-GHz Australia Telescope Large Area Survey (ATLAS) in the *Chandra* Deep Field South (CDFS), with no detected 3.6-μm counterparts in the *Spitzer* Wide-area Infrared Extragalactic Survey (SWIRE; Lonsdale et al. 2003). Further, using the ATLAS and SWIRE data, Middelberg et al. (2008) found 31 IFRSs in 3.6 deg^2

of the European Large Area IR space observatory Survey South 1 (ELAIS-S1) field. The 1.4-GHz flux density of the IFRSs found in these deep fields ranges from a few hundred μJy to a few tens of mJy, while non-detection in the SWIRE puts an upper flux limit of 5 μJy on the 3.6-μm band. Thus, the ratio of radio-to-infrared flux densities for IFRSs ranges from several hundred to several thousand, similar to that for high-redshift radio galaxies (HzRGs). However, unlike HzRGs, the faintness of IFRSs in the optical and IR bands makes it difficult to unveil their true nature. Notably, all 53 IFRSs found in the ATLAS also lacked optical counterparts, which suggests that they are extreme counterparts of optically invisible radio sources (OIRSs) identified by Higdon et al. (2005). The OIRSs are compact radio sources with no detected optical counterparts up to the *R*-band magnitude of 25.7. Higdon et al. (2008) reported that a substantial fraction (34 per cent) of OIRSs also lacked counterparts in the 3.6-μm band, and suggested that they are possible candidates for HzRGs ($z > 2$).

★ E-mail: veeresh.iia@gmail.com (VS); yogesh@ncra.tifr.res.in (YW);
ishwar@ncra.tifr.res.in (CHI-C)

Given the faintness of optical and IR counterparts of IFRSs, the initial investigations of IFRSs were limited to radio wavelengths. For example, many IFRSs have been detected with very long baseline interferometry (VLBI), which inferred high brightness temperature (T_B) $\sim 10^6$ K (see Norris et al. 2007; Middelberg et al. 2008; Herzog et al. 2015a). The IFRSs were also found to exhibit radio spectra steeper ($\alpha < -1$) than the general radio population (Middelberg et al. 2011). Several IFRSs also showed polarization in radio, which suggests that they are active galactic nuclei (AGNs) rather than star-forming galaxies (SFGs; Banfield et al. 2011; Middelberg et al. 2011; Collier et al. 2014). In an attempt to detect IR counterparts of IFRSs, Huynh et al. (2010) used ultra-deep *Spitzer* imaging in the extended *Chandra* Deep Field South (eCDFS) and reported the detection of only two IFRSs that have 3.6 µm fluxes 5.5 ± 0.3 and 6.6 ± 0.3 µJy. The fainter IFRS of these two also showed an optical counterpart with $V_{AB} = 26.27$ and $z_{AB} = 25.62$ in the optical Advanced Camera for Surveys (ACS; Giavalisco et al. 2004) images. Using one of the deepest *Spitzer* imaging surveys, the *Spitzer* Extragalactic Representative Volume Survey (SERVS; Mauduit et al. 2012) with a 3σ flux limit of 1.5 µJy beam^{-1}, Norris et al. (2011b) reported candidate detections of only three ATLAS IFRSs – with the possibility that they are spurious detections due to noise. The stacking of SERVS image cut-outs at the radio positions of IFRSs resulted in a median flux density of $\leq$0.2 µJy beam^{-1}, which, in turn, suggests the extreme ratio of radio-to-3.6-µm flux densities for IFRSs.

One of the most important aspects of the study of IFRSs is to estimate their redshifts. However, in most cases, it has been difficult to estimate the redshifts of IFRSs because of the faintness of their optical and IR counterparts. The lack of redshift causes a major hindrance in understanding their nature, including basic properties such as distance, physical size, luminosity and cosmological epoch. We note that Zinn, Middelberg & Ibar (2011) presented a catalogue of 55 IFRSs in four deep fields (i.e. CDFS, ELAIS-S1, FLS and COSMOS), but without redshift estimates. Furthermore, using the Unified Radio Catalogue (URC; Kimball & Ivezić 2008) and the *Wide-Field Infrared Survey Explorer* (*WISE*; Wright et al. 2010) data, Collier et al. (2014) presented a catalogue of 1317 IFRSs that are suggested to be closer version of IFRSs found in the deep surveys, but only 18/1317 (1.3 per cent) of IFRSs have spectroscopic redshifts ($2 < z < 3$) from the Sloan Digital Sky Survey (SDSS). In order to obtain redshifts of IFRSs, Herzog et al. (2014) carried out spectroscopic observations with the Very Large Telescope (VLT) for four IFRSs selected by their relatively bright optical counterparts ($m_r \sim 22.0$–24.1 in Vega) and found spectroscopic redshifts of only three IFRSs.

Indeed, despite several attempts, the nature of the IFRS population remains unclear, mainly because of their non-detection in the optical and IR bands. Therefore, obtaining more sensitive optical and IR observations of radio surveyed fields is key to understanding the nature of IFRSs. The Subaru X-ray Deep Field (SXDF) and Very Large Array–VIMOS VLT Deep Survey (VLA-VVDS) fields possess deep multiwavelength – i.e. radio, optical, NIR, mid-infrared (MIR), far-infrared (FIR) and X-ray – data, and therefore both fields are advantageous for investigating the nature of IFRSs. Also, the availability of deep 1.4-GHz (5σ = 100 µJy beam^{-1}) and 3.6-µm (5σ $\simeq$ 1.3–2.0 µJy beam^{-1}) data in both fields allows us to identify the IFRS population at fainter flux levels. In this paper, we identify and investigate the nature of IFRSs, in the relatively fainter flux regime, in the SXDF and VLA-VVDS fields.

Details about the existing multiwavelength data in the two fields are given in Section 2. The selection criteria and the sample of

our IFRSs are described in Section 3. In Section 4, we present redshift estimates of our IFRSs. Section 5 is devoted to a comparison between our sample and previously reported IFRS samples. The radio properties of our IFRSs are discussed in Section 6, and the properties of multiwavelength counterparts of IFRSs are discussed in Section 7. The results and conclusions of our study are summarized in Section 8. The cosmological parameters used in this paper are $H_0 = 71$ km s^{-1} Mpc^{-1}, $\Omega_M = 0.27$ and $\Omega_\Lambda = 0.73$. In the ΛCDM cosmology, the linear scale spans a limited range between 4 and 8.5 kpc arcsec^{-1} in the redshift range of $0.5 \leq z \leq 12$. All magnitudes are listed in the AB system unless mentioned otherwise.

2 MULTIWAVELENGTH DATA

Both the SXDF (centred at RA = 02^h 18^m 00^s and Dec. = −05° 00′ 00″ with a total area of 1.3 deg^2; Furusawa et al. 2008) and the VLA-VVDS (centred at RA = 02^h 26^m 00^s and Dec. = −04° 30′ 00″ with a total area of 1.0 deg^2; Le Fèvre et al. 2004) fields are defined on the basis of area covered by the deep optical surveys from Subaru and VLT, respectively. Both the optically surveyed fields have also been fully or partially surveyed at other wavelengths ranging from radio, IR to X-ray. The multiwavelength data available in the two fields are listed in Table 1, and the footprints of these multiwavelength surveys are shown in Fig. 1. Because the identification of IFRSs is based on the search for 3.6-µm counterparts of 1.4-GHz radio sources (see Section 3), we begin with 1.4-GHz VLA radio source catalogues that cover 0.8/1.3 deg^2 in the central region of the SXDF and a full 1.0 deg^2 in the VLA-VVDS. The search for our IFRSs is further limited to the common area (0.8 deg^2 in the SXDF and 0.96 deg^2 in the VLA-VVDS) covered by both the radio and 3.6-µm surveys. The multiwavelength counterparts of IFRSs are searched from the deepest available data in the overlapped regions.

In the following subsections, we provide brief details about the available multiwavelength data. The footprints of some surveys (e.g. 1.4 GHz, 610 MHz, X-ray) are matched with the optical coverage, and therefore, in such cases, we do not provide the survey coordinates repeatedly.

2.1 Radio data

2.1.1 1.4-GHz VLA surveys

SXDF. The full 1.3-deg^2 area of the SXDF was surveyed at 1.4 GHz using the VLA 'BnC' configuration (Simpson et al. 2006). The mosaicked 1.4-GHz radio map, made from 14 overlapping pointings arranged in a hexagonal pattern, has nearly uniform rms noise of 20 µJy beam^{-1} in the central 0.8 deg^2 while it increases in the peripheral regions. Based on these data, Simpson et al. (2006) presented a catalogue of 512 radio sources with a detection limit of 5σ = 100 µJy beam^{-1} in the central 0.8 deg^2. The VLA radio map has a synthesized beam size of 5.0×4.0 arcsec^2 with position angle (PA) 170°.

VLA-VVDS. Bondi et al. (2003) carried out a 1.4-GHz VLA 'B' survey of the full 1.0 deg^2 of the VLA-VVDS field. Their nine-pointing mosaicked radio map of the full field has nearly uniform rms noise of 17 µJy beam^{-1} and a resolution of 6.0 arcsec. The survey resulted in a total of 1054 radio sources detected above 5σ limit.

Table 1. Summary of the multiwavelength data. The total area of surveys having coverages outside the deep fields are given within parentheses. The values for the area and sensitivity of different surveys are rounded to the first decimal place. Radio surveys from VLA and GMRT have no specific names. The optical surveys SXDS, VVDS and CFHTLS-D1 are carried out with the Suprime-Cam/Subaru, CFH12K/VLT and MegaCam/CFHT, respectively. The UDS and VIDEO NIR surveys are based on the UKIRT Wide-Field Camera (WFCAM) and VISTA IR Camera (VIRCAM), respectively. *Spitzer* surveys (SpUDS, SERVS, SWIRE) in MIR (3.6, 4.5, 5.0 and 8.0 μm) and FIR (24 and 70 μm) bands are from IRAC and MIPS, respectively. In HerMES, 110- and 160-μm observations are from PACS, while 250-, 350- and 500-μm observations are from SPIRE. In X-ray, the SXDS and XMDS surveys are carried out with the *XMM–Newton*.

| Band	SXDF				VLA-VVDS			
	Survey	5σ Depth (unit)	Area (deg²)	Reference[a]	Survey	5σ Depth (unit)	Area (deg²)	Reference[a]
Radio		(μJy beam⁻¹)				(μJy beam⁻¹)		
1.4 GHz	VLA	100	0.8	1	VLA	80	1.0	2
610 MHz					GMRT	250	1.0	3
325 MHz	GMRT	750	0.8 (12.0)	4	GMRT	750	1.0 (12.0)	4
Optical		(mag)				(mag)		
B	SXDS	28.4	0.8	5	VVDS	26.5	1.0	6
V	SXDS	27.8	0.8	5	VVDS	26.2	1.0	6
R	SXDS	27.7	0.8	5	VVDS	25.9	1.0	6
I					VVDS	25.0	1.0	6
$u^\star$					CFHTLS D1	26.5	1.0	7
g'					CFHTLS D1	26.4	1.0	7
r'					CFHTLS D1	26.1	1.0	7
i'	SXDS	27.7	0.8	5	CFHTLS D1	25.9	1.0	7
z'	SXDS	26.6	0.8	5	CFHTLS D1	25.0	1.0	7
NIR								
Z					VIDEO	25.7	1.0 (4.5)	9
Y					VIDEO	24.5	1.0 (4.5)	9
J	UDS	25.6	0.6 (0.8)	8	VIDEO	24.4	1.0 (4.5)	9
H	UDS	25.1	0.6 (0.8)	8	VIDEO	24.1	1.0 (4.5)	9
K	UDS	25.3	0.6 (0.8)	8	VIDEO	23.8	1.0 (4.5)	9
MIR								
3.6 μm	SpUDS	24.0	0.6 (1.0)	10				
	SERVS	23.1	0.7 (4.5)	11	SERVS	23.1	0.8 (4.5)	11
		(μJy beam⁻¹)				(μJy beam⁻¹)		
	SWIRE	7.3	0.8 (9.0)	12	SWIRE	7.3	0.9 (9.0)	12
		(mag)				(mag)		
4.5 μm	SpUDS	23.9	0.6 (1.0)	10	SERVS	23.1	0.8 (4.5)	11
		(μJy beam⁻¹)				(μJy beam⁻¹)		
5.8 μm	SpUDS	8.5	0.6 (1.0)	10	SWIRE	27.5	0.9 (8.7)	12
8.0 μm	SpUDS	10.5	0.6 (1.0)	10	SWIRE	32.5	0.9 (8.7)	12
FIR		(mJy)				(mJy)		
24 μm	SpUDS	0.1	0.6 (1.0)	10	SWIRE	0.45	0.9 (9.0)	12
70 μm						2.75	0.9 (9.0)	12
110 μm	HerMES	11.2	0.8 (4.2)	13	HerMES	28.8	1.0 (6.2)	13
160 μm	HerMES	21.4	0.8 (4.2)	13	HerMES	54.9	1.0 (6.2)	13
250 μm	HerMES	11.2	0.8 (4.2)	13	HerMES	11.2	1.0 (6.2)	13
350 μm	HerMES	9.3	0.8 (4.2)	13	HerMES	9.3	1.0 (6.2)	13
500 μm	HerMES	13.4	0.8 (4.2)	13	HerMES	13.4	1.0 (6.2)	13
X-ray		(erg cm⁻² s⁻¹)				(erg cm⁻² s⁻¹)		
0.5–2.0 keV	SXDS	6×10^{-16}	0.8 (1.1)	14	XMDS	1×10^{-15}	1.0 (3.0)	15
2.0–10 keV	SXDS	3×10^{-15}	0.8 (1.1)	14	XMDS	7×10^{-15}	1.0 (3.0)	15

Notes. [a]References are: 1, Simpson et al. (2006); 2, Bondi et al. (2003); 3, Bondi et al. (2007); 4, Wadadekar et al. (in preparation); 5, Furusawa et al. (2008); 6, Ciliegi et al. (2005); 7, Ilbert et al. (2006); 8, Lawrence et al. (2007); 9, Jarvis et al. (2013); 10, Dunlop et al. (2007); 11, Mauduit et al. (2012); 12, Lonsdale et al. (2003); 13, Oliver et al. (2012); 14, Ueda et al. (2008); 15, Chiappetti et al. (2005).

2.1.2 610-MHz GMRT survey

The VLA-VVDS field has also been surveyed at 610 MHz with the Giant Metrewave Radio Telescope (GMRT), although there are no deep 610-MHz observations in the SXDF. The 610-MHz GMRT survey of the VLA-VVDS covers a full 1.0 deg² with a sensitivity limit of 250 μJy beam⁻¹ at the 5σ level and a resolution of 6.0 arcsec (Bondi et al. 2007). There are a total of 514 radio sources detected at ≥5σ in 1.0 deg².

2.1.3 325-MHz GMRT survey

Both the SXDF and VLA-VVDS fields also lie within the 325-MHz GMRT survey (centred at RA = 02^h 21^m 00^s and Dec. = −04° 30′ 00″) of 12 deg² covered with 16 pointings, in the *XMM–Newton* Large-Scale Structure (*XMM*-LSS) field (Wadadekar et al., in preparation). The 325-MHz GMRT mosaicked image, with a synthesized beam size of 9.4 × 7.4 arcsec², has an average rms noise of 150 μJy beam⁻¹ and it reaches down to 120 μJy beam⁻¹
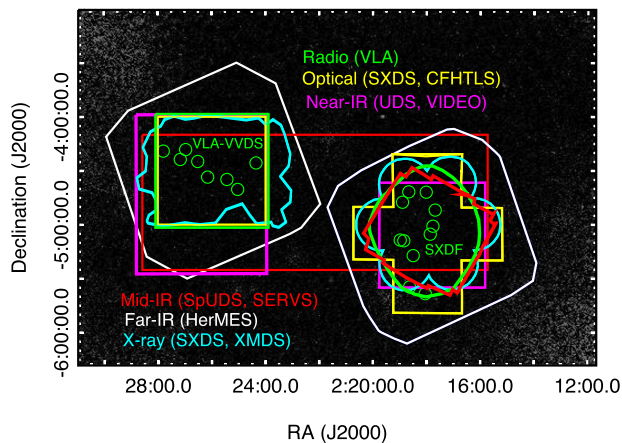
Figure 1. The footprints of deep multiwavelength surveys (i.e. 1.4-GHz radio in green, optical in yellow, NIR in magenta, MIR in red, FIR in white and X-ray in cyan) in the SXDF (right side) and VLA-VVDS (left side) overplotted on to a part of the 325-MHz GMRT image. The footprints of large area surveys (i.e. SWIRE and 325-MHz GMRT) that cover both the deep fields are not shown here. The positions of our IFRSs are indicated by green circles.

in the central region. The 325-MHz GMRT survey is the deepest low-frequency radio survey in the *XMM*-LSS field, and detects a total of 3304 radio sources at $\geq 5\sigma$ with a noise cut-off ≤ 300 μJy. We already used these 325-MHz GMRT data in combination with the existing multiwavelength data to study ultra-steep spectrum (USS) radio sources (Singh et al. 2014), the radio–FIR correlation for distant SFGs (Basu et al. 2015) and a giant relic radio galaxy at $z \sim 1.3$ (Tamhane et al. 2015).

2.2 Optical data

SXDF. The optical data are obtained from the Subaru/*XMM–Newton* Deep Survey (SXDS), which is carried out with the Suprime-Cam on the Subaru telescope (Furusawa et al. 2008). The SXDS provides photometric data in B, V, R_c, i' and z' bands to the 5σ depths of 28.4, 27.8, 27.7, 27.7 and 26.6 mag, respectively. Using the SXDS data, Simpson et al. (2006) present the optical identifications of 1.4-GHz radio sources.

VLA-VVDS. The full 1.0 deg^2 of the VLA-VVDS was covered by the VVDS and the Canada–France–Hawaii Telescope Legacy Survey D1 field (CFHTLS D1). The CFHTLS D1 provides photometric observations in $u^\star$, g', r', i' and z' bands to the 5σ depths of 26.5, 26.4, 26.1, 25.9 and 25.0 mag, respectively (Ilbert et al. 2006). The VVDS carried out with the CFH12K wide-field mosaic camera yields optical photometric data in B, V, R and I bands to the 5σ limiting magnitudes (50 per cent completeness for point sources) of $B = 26.5$, $V = 26.2$, $R = 25.9$ and $I = 25.0$ (see McCracken et al. 2003). The 5σ limiting magnitudes at 90 per cent completeness are nearly one magnitude brighter ($I = 24.0$).

2.3 NIR data

SXDF. 0.63 deg^2 of the SXDF is covered by the Ultra Deep Survey (UDS) from the UKIRT Infrared Deep Sky Survey (UKIDSS; Lawrence et al. 2007). The UDS is centred at RA $= 02^h 17^m 48^s$ and Dec. $= -05° 06' 00''$ (J2000) and covers a total area of 0.77 deg^2. The magnitude limits of the UDS DR 11 at 5σ level are $J = 25.6$, $H = 25.1$ and $K = 25.3$

VLA-VVDS. The NIR VISTA Deep Extragalactic Observations (VIDEO; Jarvis et al. 2013) survey covers the full 1.0 deg^2 of the VLA-VVDS field. In the *XMM*-LSS field, the VIDEO survey covers a total area of 4.5 deg^2 that is subdivided into three tiles, each covering 1.5 deg^2. The VIDEO survey provides photometric observations in Z, Y, J, H and K_s bands with 5σ magnitude limits of 25.7, 24.5, 24.4, 24.1 and 23.8, respectively.

2.4 MIR data

SXDF. The MIR data in the SXDF are available from the *Spitzer* Public Legacy survey of the UKIDSS Ultra Deep Survey (SpUDS; Dunlop et al. 2007), which was carried out with all four IRAC bands (3.6, 4.5, 5.8 and 8.0 μm) and one MIPS band (24 μm). The SpUDS covers the full 0.8 deg^2 of the UDS and 0.6 deg^2 of the SXDF with 5σ detection limits of $[3.6] = 24.0$ (1.3 μJy beam^{-1}) and $[4.5] = 23.9$ (1.7 μJy beam^{-1}).

VLA-VVDS. Nearly 0.82 deg^2 out of the total 1.0 deg^2 of the VLA-VVDS field is covered by the *Spitzer* Extragalactic Representative Volume Survey (SERVS; Mauduit et al. 2012), which is a medium deep survey at 3.6 and 4.5 μm with a 5σ sensitivity limit of 23.1 mag (2.0 μJy beam^{-1}) in both bands. The SERVS covers a total area of 4.5 deg^2 in the *XMM*-LSS field and is centred at RA $= 02^h 20^m 00^s$ and Dec. $= -04° 48' 00''$ (J2000).

SERVS also covers 0.6/0.8 deg^2 of the radio coverage in the SXDF. Furthermore, both SXDF and VLA-VVDS have substantial overlap with the SWIRE (Lonsdale et al. 2003), which is centred at RA $= 02^h 21^m 00^s$ and Dec. $= -04° 30' 00''$ (J2000) and covers a total of 8.7 deg^2 in all four IRAC bands (3.6, 4.5, 5.8 and 8.0 μm) and 9.0 deg^2 in MIPS bands (24, 70 and 160 μm), with 5σ sensitivity of 7.3, 9.7, 27.5 and 32.5 μJy beam^{-1} in the four IRAC bands, respectively, and 0.45, 2.75 and 17.5 mJy beam^{-1} in three MIPS bands, respectively.

2.5 FIR data

Both the SXDF and VLA-VVDS fields are fully covered by the *Herschel*/SPIRE surveys that are part of the level-4 *Herschel* Multitiered Extragalactic Survey (HerMES; Oliver et al. 2012). The level-4 HerMES observations were carried out at 250, 350 and 500 μm bands with 5σ sensitivity limits of 11.2, 9.3 and 13.4 mJy beam^{-1}, respectively. These *Herschel* surveys are centred at the optically surveyed fields and cover an area of 2.0 deg^2 in each field.

2.6 X-ray data

SXDF. The SXDS covers a total area of 1.14 deg^2 centred at RA $= 02^h 18^m 00^s$ and Dec. $= -05° 00' 00''$ (Ueda et al. 2008). It consists of one central 30-arcmin diameter field with a 100-ks exposure time and six flanking fields with 50-ks exposure time. The SXDS presents a catalogue of 866 and 645 X-ray sources with sensitivity limits of 6.0×10^{-16} and 3.0×10^{-15} erg cm^{-2} s^{-1} in the 0.5–2.0 and 2.0–10 keV bands, respectively, with detection likelihood of ≥ 7 (corresponding to a confidence level of 99.9 per cent).

VLA-VVDS. The *XMM* Medium Deep Survey (XMDS) covers the central region of the *XMM*-LSS field and provides a catalogue of 286 sources detected at 4σ in the 1 deg^2 area of the VLA-VVDS field (Chiappetti et al. 2005). The XMDS covers a contiguous area of about 3 deg^2 over 19 pointings (typical exposure time of

Table 2. The IFRS sample. The radio luminosities are in the rest frame with *K*-correction applied. In the redshift column, '(s)' denotes a spectroscopic redshift.

RA (h m s)	Dec. (° ′ ″)	$S_{1.4\,GHz}$ (mJy)	Radio size (arcsec (kpc))	$S_{3.6\,\mu m}$ (μJy)	$S_{1.4\,GHz}/S_{3.6\,\mu m}$	$S_{610\,MHz}$ (mJy)	$S_{325\,MHz}$ (mJy)	$\alpha^{1.4\,GHz}_{325\,MHz}$	Redshift (z)	$L_{1.4\,GHz}$ (W Hz^{-1})
SXDF										
02 18 39.55	−04 41 49.4	50.82 ± 0.07	21 (173)	13.63 ± 0.254^a	3727.4	–	250 ± 3.5	− 1.09 ± 0.01	2.43(s)	2.73 × 10^{27}
02 17 52.12	−05 05 22.4	6.19 ± 0.05	≤ 1.22 (9.6)	3.20 ± 0.254^a	1934.4	–	2.65 ± 0.4	0.58 ± 0.05	2.92	5.35 × 10^{25}
02 18 53.63	−04 47 35.6	16.95 ± 0.07	≤ 1.53 (12.6)	27.84 ± 0.254^a	608.8	–	22.8 ± 0.8	− 0.20 ± 0.02	2.47(s)	3.12 × 10^{26}
02 18 51.38	−05 09 01.6	16.01 ± 0.07	≤ 1.11 (9.5)	29.82 ± 0.268^a	536.9	–	62.5 ± 1.0	− 0.93 ± 0.01	1.75	3.18 × 10^{26}
02 18 03.41	−05 38 25.5	8.91 ± 0.09	≤ 2.57 (19.0)	13.90 ± 0.97^a	641	–	28.4 ± 0.2	− 0.79 ± 0.01	3.57(s)	7.92 × 10^{26}
02 18 38.24	−05 34 44.2	1.58 ± 0.02	≤ 2.19 (18.7)	<7.3^b	>216	–	9.7 ± 0.2	− 1.24 ± 0.02	1.68	3.85 × 10^{25}
02 17 40.69	−04 51 57.3	0.526 ± 0.047	14 (96)	<1.3^a	>405	–	4.2 ± 0.5	− 1.42 ± 0.01	4.32	2.04 × 10^{25}
02 17 45.84	−05 00 56.4	0.589 ± 0.013	≤ 1.58 (13.2)	<1.3^a	>453	–	5.4 ± 0.4	− 1.52 ± 0.01	2.22	4.15 × 10^{25}
02 18 01.23	−04 42 00.8	0.109 ± 0.013	≤ 4.64 (39.7)	<1.3^a	>84	–	0.19 ± 0.12	− 0.38 ± 0.01	1.72	1.19 × 10^{24}
02 18 30.13	−05 17 17.4	0.187 ± 0.013	≤ 2.98 (25.2)	<1.3^a	>144	–	0.59 ± 0.13	− 0.79 ± 0.01	2.04	4.59 × 10^{24}
02 18 59.19	−05 08 37.8	0.698 ± 0.014	≤ 1.58 (11.6)	<1.3^a	>537	–	0.23 ± 0.12	0.76 ± 0.02	3.60	5.90 × 10^{24}
VLA-VVDS										
02 27 48.26	−04 19 05.3	0.162 ± 0.017	≤ 3.3 (27.9)	<2.0^c	>81	<0.25	0.67 ± 0.15	− 0.97 ± 0.01	>2.0	>4.63 × 10^{24}
02 25 02.13	−04 40 26.9	0.202 ± 0.030	≤ 5.74 (48.6)	<2.0^c	>101	<0.25	0.54 ± 0.11	− 0.67 ± 0.01	>2.0	>4.16 × 10^{24}
02 26 58.10	−04 18 14.9	0.217 ± 0.016	≤ 5.06 (42.9)	<2.0^c	>109	0.68 ± 0.05	2.72 ± 0.46	− 1.71 ± 0.01	>2.0	>1.43 × 10^{25}
02 27 09.90	−04 23 44.8	0.238 ± 0.016	≤ 3.2 (27.1)	<2.0^c	>119	0.61 ± 0.05	1.51 ± 0.13	− 1.26 ± 0.01	>2.0	>9.48 × 10^{24}
02 26 31.12	−04 24 53.3	0.699 ± 0.066	18 (152.6)	<2.0^c	>350	1.71 ± 0.15	4.56 ± 0.58	− 1.27 ± 0.01	>2.0	>2.81 × 10^{25}
02 25 26.14	−04 34 54.4	1.392 ± 0.049	28 (237)	<2.0^c	>696	1.87 ± 0.05	3.4 ± 0.5	− 0.60 ± 0.01	>2.0	>1.78 × 10^{25}
02 26 09.09	−04 33 34.7	8.643 ± 0.020	≤ 2.76 (22.7)	<2.0^c	>4321	18.10 ± 0.05	31.8 ± 0.7	− 0.89 ± 0.01	2.45	3.68 × 10^{26}
02 24 20.96	−04 25 44.6	18.967 ± 0.025	39 (330.5)	1.8 ± 0.3^c	10537	50.56 ± 0.10	108.8 ± 1.0	− 1.20 ± 0.01	>2.0	>7.0 × 10^{26}

Notes. ^{a}SpUDS.
^{b}SWIRE.
^{c}SERVS.

∼20–25 ks) and reaches down to flux limits of 1.0×10^{-15} erg cm^{-2} s^{-1} in the 0.5–2.0 keV band and 7.0×10^{-15} erg cm^{-2} s^{-1} in the 2.0–10 keV band at 4σ level.

3 IDENTIFICATION OF IFRSs

3.1 Selection criteria

In order to identify IFRSs, we adopt the selection criteria proposed by Zinn et al. (2011) and select a radio source as an IFRS if the following two conditions are satisfied: (i) $S_{1.4\,GHz}/S_{3.6\,\mu m} > 500$; (ii) $S_{3.6\,\mu m} < 30\,\mu Jy$ (including a non-detection). The first criterion allows us to mitigate the contamination from foreground stars and SFGs, owing to the well-known radio–IR correlation (Appleton et al. 2004), whereas the second criterion helps us to exclude low-redshift radio sources that tend to be relatively bright in IR. For instance, Cygnus A ($S_{1.4\,GHz}/S_{3.6\,\mu m} = 2 \times 10^5$), a nearby radio galaxy, would be selected as an IFRS based on the first criterion, while it would be excluded based on the second criterion. It is worth mentioning that the limiting values used in the IFRS selection criteria are arbitrary but select almost all the known IFRSs ranging from faint to bright ones (see Zinn et al. 2011; Collier et al. 2014).

For radio sources with undetected 3.6-μm counterparts, we have only a lower limit on the flux ratio of 1.4 GHz to 3.6 μm ($S_{1.4\,GHz}/S_{3.6\,\mu m}$), and such sources can be potential candidates for IFRSs. The non-detection of 3.6-μm counterparts in the SpUDS, SERVS and SWIRE surveys gives $S_{3.6\,\mu m} < 30\,\mu Jy$ (see Table 1). Therefore, we include candidate IFRSs in our sample and define them as follows: (i) radio sources with no detected 3.6-μm counterparts and (ii) the lower limit on $S_{1.4\,GHz}/S_{3.6\,\mu m}$ is less than 500. A radio source with an undetected 3.6-μm counterpart but having limiting value of the flux ratio of 1.4 GHz to 3.6 μm ($S_{1.4\,GHz}/S_{3.6\,\mu m}$) > 500 becomes a confirmed IFRS.

We note that, to ensure the reliability of our IFRSs, we have excluded faint radio sources with a signal-to-noise ratio (S/N) < 8

and we have also discarded multicomponent extended radio sources with an ambiguous centroid position. We thereby ensure that a spurious radio source is not identified as an IFRS.

3.2 The sample

With the selection criteria outlined above, we find six confirmed and five candidate IFRSs in the SXDF field, and three confirmed and five candidate IFRSs in the VLA-VVDS field. In total, we find nine confirmed and ten candidate IFRSs in the two fields. All our IFRSs and their basic parameters are listed in Table 2. The detailed procedure used for the identification of our IFRSs is given below. To find 3.6-μm counterparts of 1.4-GHz radio sources, we give first priority to the deepest available 3.6-μm survey (i.e. SpUDS, SERVS and SWIRE in decreasing order of priority).

3.2.1 Identification of IFRSs in the SXDF

To identify IFRSs in the SXDF, we first search for 3.6-μm counterparts of 1.4-GHz radio sources by cross-matching the 3.6-μm and 1.4-GHz source catalogues. There are a total of 512 1.4-GHz radio sources over 0.8 deg^2, of which 0.63 deg^2 is covered by the 3.6-μm SpUDS survey that contains only 438 radio sources (see Fig. 1). We cross-matched 1.4-GHz radio and 3.6-μm IR sources using a search radius of 5.0 arcsec around the radio positions. This exercise yielded 428/438 cross-matched sources, where a majority of sources (401/428 ∼ 93.7 per cent) were matched within 1.0 arcsec. Sources with larger positional offset (>1.0 arcsec) are generally fainter in radio as well as in 3.6 μm and seem to suffer from larger positional uncertainties. The chosen search radius of 5.0 arcsec corresponds to a projected linear distance of ≤45 kpc at a redshift (z) > 0.5, which is the typical size of a galaxy. We estimate the flux ratio of 1.4 GHz to 3.6 μm for all the cross-matched sources, and find that only five out of 428 radio sources

satisfy our IFRS selection criteria (i.e. $S_{1.4\,GHz}/S_{3.6\,\mu m} > 500$ and $S_{3.6\,\mu m} < 30\,\mu Jy$).

For the 10 radio sources with no cross-matched 3.6-μm counterparts, we visually inspected the 3.6-μm SpUDS image cut-outs centred at their radio positions. We found that five radio sources are falling either on or close to bright extended foreground IR sources, which makes the identification of true 3.6-μm counterparts difficult. This leaves us with only five radio sources with undetected 3.6-μm counterparts ($S_{3.6\,\mu m} < 1.3\,\mu Jy$). With the estimated lower limits on the ratio of 1.4 GHz to 3.6 μm, one of the five radio sources turns out to be a confirmed IFRS ($S_{1.4\,GHz}/S_{3.6\,\mu m} > 537$), while the remaining four radio sources that have $S_{1.4\,GHz}/S_{3.6\,\mu m} \simeq 84$–$453$ can be considered candidate IFRSs (see Table 2). Thus, within the SpUDS coverage, we find only six confirmed IFRSs and four candidate IFRSs. We note that among 74/512 radio sources falling outside the SpUDS coverage, 28/74 radio sources are covered within the SERVS footprint, while the remaining 46/74 radio sources are covered with the SWIRE. All 28 radio sources falling within the SERVS coverage area have 3.6-μm counterparts, but none of these sources has a flux ratio of 1.4 GHz to 3.6 μm ($S_{1.4\,GHz}/S_{3.6\,\mu m}$) >500. Among the 46 radio sources covered with the SWIRE, 43/46 radio sources have 3.6-μm counterparts, but none of these satisfies the IFRS selection criteria. Two of the three radio sources with no 3.6-μm counterparts are fairly faint in radio (i.e. S/N $\simeq 5\sigma$) and fall below our cut-off limit of S/N ≥ 8. Also, only one among three radio sources meets the criteria of candidate IFRSs with $S_{3.6\,\mu m} < 7.3\,\mu Jy$ and $S_{1.4\,GHz}/S_{3.6\,\mu m} > 216$. Therefore, using SpUDS, SERVS and SWIRE data we find, in total, only six confirmed IFRSs and five candidate IFRSs in the SXDF (see Table 2).

3.2.2 Identification of IFRSs in the VLA-VVDS

The VLA-VVDS field contains a total of 1054 1.4-GHz radio sources in a 1.0 deg^2 area, of which only 0.82 deg^2 (containing 865/1054 radio sources) overlaps with the SERVS. The cross-matching of 1.4-GHz and 3.6-μm source catalogues using a search radius of 5.0 arcsec around the radio position yielded 3.6-μm counterparts for only 789/865 (91.2 per cent) radio sources. We find that none of these 789 cross-matched radio sources meets the IFRS selection criteria (i.e. $S_{1.4\,GHz}/S_{3.6\,\mu m} > 500$ and $S_{3.6\,\mu m} \leq 30\,\mu Jy$). For the remaining 76/865 radio sources with no cross-matched counterparts, we visually inspected the 3.6-μm SERVS image cut-outs centred at the radio positions. We excluded all the radio sources that lie on or close to bright extended foreground IR sources, which do not allow us to find the true 3.6-μm counterparts. We also excluded faint radio sources with S/N < 8 and multicomponent extended radio sources with ambiguous centroid positions. This exercise yielded only eight radio sources with no detected 3.6-μm counterparts. Only three among these eight radio sources are considered to be confirmed IFRSs with the limiting flux ratio $S_{1.4\,GHz}/S_{3.6\,\mu m} > 500$, while the remaining five radio sources can only be considered as candidate IFRSs (see Table 2). One among three confirmed IFRSs has a 3.6-μm counterpart just below 5σ with $S_{3.6\,\mu m} \sim 1.8 \pm 0.3\,\mu Jy$. 142 out of 189/1054 radio sources that are not covered by the SERVS fall within the SWIRE coverage, while the remaining 47/189 radio sources are not covered by any 3.6-μm survey. Cross-matching of 142 radio sources with the 3.6-μm SWIRE catalogue yielded 3.6-μm counterparts for 130 radio sources, but none of these satisfies our IFRS selection criteria. Eight out of 12/142 radio sources with no 3.6-μm counterparts are faint

and fall below our S/N cut-off limit (S/N ≥ 8). Visual inspection of the 3.6-μm SWIRE image cut-outs shows that the remaining four sources have counterparts at offset > 5.0 arcsec. The larger positional offset may be because these radio sources are extended. Considering the nearest 3.6-μm counterparts, none of these radio sources meets our IFRS selection criteria. Therefore, using SERVS and SWIRE data we find, in total, only three confirmed IFRSs and five candidate IFRSs in the VLA-VVDS field. We caution that our IFRS sample can suffer from incompleteness, in particular, at fainter flux densities.

4 REDSHIFT ESTIMATES

One the most important aspects in the study of IFRSs is to estimate their redshifts. We attempt to obtain the redshift estimates of our IFRSs by using the existing data available in the literature (see Table 2). The details about the redshift estimates in both fields are given below.

SXDF. The redshift estimates of our sample sources are obtained mainly from Simpson et al. (2012) who reported the spectroscopic and/or photometric redshifts of 505/512 1.4-GHz radio sources. The spectroscopic redshift estimates of 267/505 radio sources are based on the observations carried out with the Visible Multi-Object Spectrograph (VIMOS) on the VLT and also include estimates from previous spectroscopic campaigns (e.g. Geach et al. 2007; Smail et al. 2008; van Breukelen et al. 2009; Banerji et al. 2011; Chuter et al. 2011). The remaining 238/505 radio sources have photometric redshift estimates derived using 11-band ($u^\star$, B, V, R, i', z', J, H, K, [3.6] and [4.5]) photometric data with the code EASY (Brammer, van Dokkum & Coppi 2008). The accuracy of the photometric redshifts is determined by comparing the photometric and spectroscopic redshifts of 267 sources. It is shown that the photometric redshift estimates are fairly accurate with the normalized median absolute deviation ∼0.035 for the histogram of normalized photometric redshift errors ($z_{phot} - z_{spec}$)/($1 + z_{spec}$). There are only 07/512 radio sources with no redshift estimates because of the presence of bright foreground objects in their close vicinity in the optical and IR images. Using the Simpson et al. (2012) measurements, we find that, among 11 IFRSs in the SXDF, only three have spectroscopic redshift estimates and eight have photometric redshift estimates (see Table 2). We note that, based on the optical spectra, Simpson et al. (2012) classify one of our IFRSs, J021839−044149, as a narrow-line AGN, while two other IFRSs (i.e. J021853−044735 and J021803−053825) are also possibly narrow-line AGNs, although with some degree of ambiguity because of the poor quality of their spectra. The optical spectra of these IFRSs are presented in Simpson et al. (2012).

VLA-VVDS. The redshift estimates of our IFRSs in the VLA-VVDS field are obtained from McAlpine, Jarvis & Bonfield (2013) who present photometric redshifts of 942/1054 1.4-GHz radio sources using ten-band ($u^\star$, g', r', i', z', Z, Y, J, H and K_s) photometric data. The photometric redshifts are derived using the code LE PHARE6 (Ilbert et al. 2006), which fits the photometric data with spectral energy distribution (SED) templates. The accuracy of the photometric redshift estimates is assessed by comparing the photometric redshifts with the spectroscopic redshifts obtained from the VVDS (Le Fèvre et al. 2013). There are only 3.8 per cent catastrophic outliers defined as sources with $|z_{phot} - z_{spec}|/(1 + z_{spec}) > 0.15$. Because of the use of more photometric bands, the redshift estimates presented in McAlpine et al. (2013) supersede previous estimates
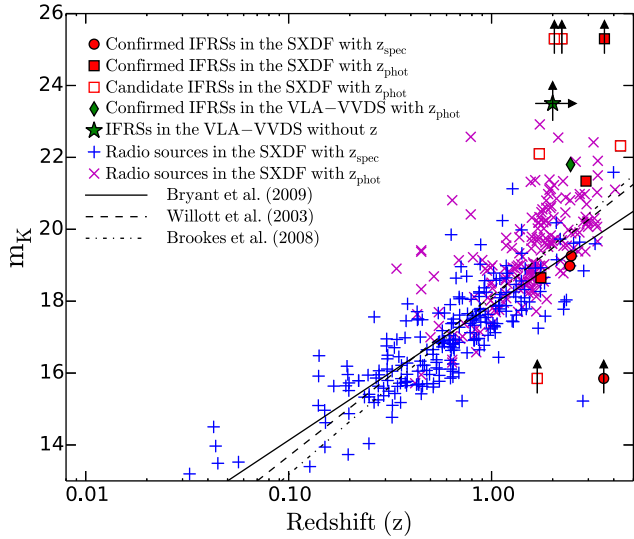
Figure 2. The locations of our IFRSs in the *K–z* plot displaying the radio sources detected in the SXDF (see Simpson et al. 2012). The vertical and horizontal arrows indicate lower limits on the *K*-band magnitudes and redshifts, respectively. Two IFRSs fall outside the UDS footprint and the lower limits ($m_K \geq 15.85$) for these two IFRSs are from 2MASS. In the VLA-VVDS field, there are seven IFRSs with no redshift and no *K*-band magnitude, and such sources are placed at $z > 2.0$ based on the trend of the *K–z* relation and the *K*-band magnitude lower limits ($m_K \geq 23.5$ from the VIDEO). The solid, dashed and dash-dotted lines represent the *K–z* relations for the samples of radio galaxies from Bryant et al. (2009), Willott et al. (2003) and Brookes et al. (2008), respectively.

(e.g. Ciliegi et al. 2005; Bardelli et al. 2009). The procedure followed for deriving the photometric redshifts is described in Jarvis et al. (2013). We also use the spectroscopic redshift catalogue produced by the VVDS, which is a magnitude-limited ($17.5 \leq i \leq 24.75$) spectroscopic redshift survey conducted by the VIMOS multislit spectrograph at the ESO-VLT (Le Fèvre et al. 2013). There are only 134/1054 1.4-GHz radio sources with spectroscopic redshifts from the VVDS. Using McAlpine et al. (2013) photometric redshift estimates together with the VVDS spectroscopic redshift catalogue, we find that only one out of eight IFRSs has a photometric redshift estimate (see Table 2).

Because seven out of eight IFRSs in the VLA-VVDS field do not have redshift estimates, we attempt to constrain the lower limits of their redshifts by using the empirical relation between the *K*-band magnitude and redshift (i.e. the *K–z* relation exhibited by radio sources). It has been found that radio galaxies at higher redshifts are systematically fainter in the *K* band (see Willott et al. 2003; Brookes et al. 2008; Bryant et al. 2009). In fact, the radio source population consisting of different types of galaxies also follows the *K–z* relation but with a relatively larger dispersion (Simpson et al. 2012). The *K* band (centred at 2.2 μm) is effective at detecting galaxies over a large redshift range ($0 < z < 4$) as it samples their NIR to optical rest-frame emission. In Fig. 2, we show the locations of our IFRSs in the *K–z* plot drawn for the 1.4-GHz radio sources detected in the SXDF. We choose radio sources from the SXDF because a large fraction (267/505 = 52.9 per cent) of these radio sources have spectroscopic redshifts, and the remaining radio sources have photometric redshifts. We find that most of our IFRSs lie at the fainter end of the *K–z* plot. Five out of 11 IFRSs detected in the SXDF do not have *K*-band counterparts, and therefore only lower limits are considered (from the UDS for three
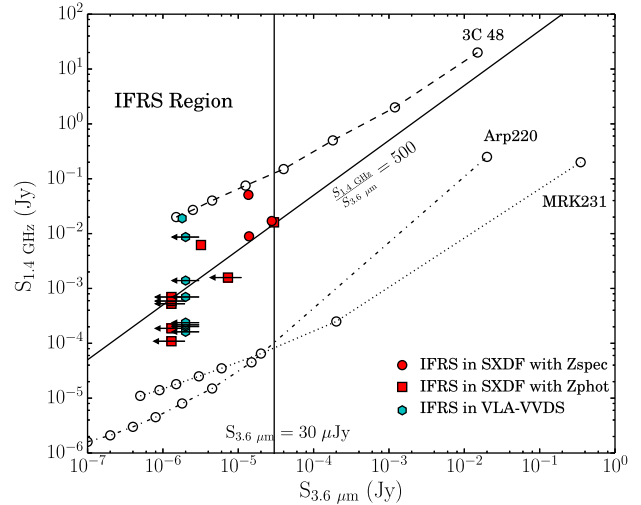

Figure 3. The locations of our IFRSs in the $S_{1.4\,\mathrm{GHz}}$ versus $S_{3.6\,\mu\mathrm{m}}$ diagnostic plot in which evolutionary tracks are shown for 3C 48 (dashed line), Arp 220 (dash-dotted line) and Mrk 231 (dotted line). The open circles represent redshifted data points with increasing redshift value from right to left, such that the first open circle having the highest flux on any track represents the current redshift of the source, the second circle represents the source placed at $z = 1$, the third circle represents the source at $z = 2$, and so on up to $z = 7$. The vertical and diagonal solid lines represent our IFRS selection criteria $S_{3.6\,\mu\mathrm{m}} < 30\,\mu\mathrm{Jy}$ and $S_{1.4\,\mathrm{GHz}}/S_{3.6\,\mu\mathrm{m}} \geq 500$, respectively. The sources above the $S_{1.4\,\mathrm{GHz}}/S_{3.6\,\mu\mathrm{m}} = 500$ line are confirmed IFRSs, while the sources below this line are candidate IFRSs.

IFRSs and from the 2MASS for two IFRSs). In the VLA-VVDS, seven IFRSs with no redshift estimates also lack *K*-band counterparts in the VIDEO data. Using *K*-band magnitude lower limits ($m_K > 23.5$ at 5σ) from the VIDEO data and the *K–z* correlation shown by the general radio population, IFRSs with no redshifts are expected to lie at $z > 2.0$ (see Fig. 2). From the *K–z* plot, it is evident that the lower limit ($z > 2.0$) on the redshifts of our IFRSs is a fairly conservative value, even if we account for the dispersion and non-linearity in the *K–z* plot, in particular at higher redshifts. The lower limit $z > 2.0$ considered for the IFRSs in the VLA-VVDS is further supported by the fact that the IFRSs with undetected *K*-band counterparts in the SXDF have estimated redshifts distributed over ~2–4. We also note that the lower limit on the redshifts is based on the *K–z* relation for faint radio sources ($5\sigma \simeq 0.1$ mJy) and these IFRSs will lie at much higher redshifts ($z > 5$) if we consider the *K–z* relation for powerful radio galaxies (e.g. $K(z) = 17.75 + 3.64\log 10(z)$; Bryant et al. 2009).

We also cross-check the accuracy of the lower limit on the redshifts of our IFRSs by using the $S_{1.4\,\mathrm{GHz}}$ versus $S_{3.6\,\mu\mathrm{m}}$ diagnostic plot (see Fig. 3). This diagnostic plot proposed by Zinn et al. (2011) shows the evolutionary tracks for three different types of galaxies: 3C 48 (a radio-loud AGN at $z = 0.37$ and a good IFRS candidate at higher redshift with $S_{1.4\,\mathrm{GHz}}/S_{3.6\,\mu\mathrm{m}} > 500$), Mrk 231 (a dusty IR bright radio-quiet AGN at $z = 0.042$) and Arp 220 (a starburst IR luminous galaxy at $z = 0.18$). In order to trace the evolution of 1.4-GHz and 3.6-μm flux density as a function of redshift, the SED templates of 3C 48, Arp 220 and Mrk 231 were redshifted to $z = 1$, 2, 3, and so on up to 7, and 1.4-GHz radio and 3.6-μm flux densities were estimated at respective redshifts. In the $S_{1.4\,\mathrm{GHz}}$ versus $S_{3.6\,\mu\mathrm{m}}$ diagnostic plot, we show the positions of our IFRSs along with the evolutionary tracks of 3C 48, Arp 220 and Mrk 231. The comparison of the positions of our IFRSs having no redshift estimates and
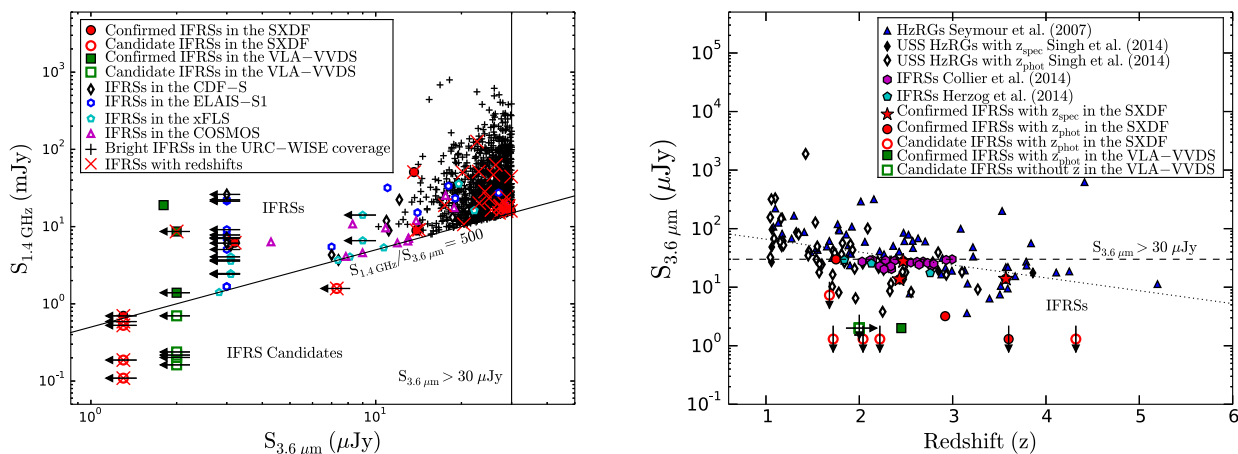
Figure 4. Left panel : $S_{1.4\,GHz}$ versus $S_{3.6\,\mu m}$ plot for IFRSs from different samples. The solid lines mark IFRS selection criteria. The horizontal arrows depict upper limits on 3.6-μm fluxes. Right panel : $S_{3.6\,\mu m}$ versus redshift plot for IFRSs and HzRGs from different samples. The horizontal dashed line marks one of the selection criteria ($S_{3.6\,\mu m} < 30\,\mu$Jy) for IFRSs. The dotted line represents the linear regression line for all confirmed IFRSs and HzRGs. Downward arrows represent the upper limits on 3.6-μm fluxes. For the Collier et al. (2014) IFRS sample, 3.4-μm flux instead of 3.6-μm flux is available from the *WISE* survey.

the evolutionary tracks of three different types of sources suggests that our IFRSs are likely to be at $z > 6.0$ if they are powerful radio-loud AGNs similar to 3C 48, and our IFRSs are at $z > 4.0$ if they are similar to Mrk 231, while our IFRSs are at $z > 2.0$ if they are similar to Apr 220. Furthermore, the locations of our IFRSs, with known redshifts at $z = 1.68$–4.3, in the $S_{1.4\,GHz}$ versus $S_{3.6\,\mu m}$ diagnostic plot, suggest that they consist of a mixed population of different types of sources ranging from powerful radio-loud AGNs to relatively less powerful radio AGNs. Indeed, the location of a source in the $S_{1.4\,GHz}$ versus $S_{3.6\,\mu m}$ plot depends on the exact nature of the SED, which is unknown for most of our IFRSs. We note that Maini et al. (2016) demonstrated the evolution of 3.6-μm flux density with redshift for different types of galaxies (e.g. Arp220, Mrk 231, type 1 and type 2 AGNs/QSOs, and radio-loud galaxies) and found that any such galaxy would lie at $z > 2.5$ if $S_{3.6\,\mu m} \leq 2.0$ μJy. Therefore, a conservative limit of $z > 2.0$ for our IFRSs with no redshift estimates, derived from the K–z relation is also consistent with their positions in the $S_{1.4\,GHz}$ versus $S_{3.6\,\mu m}$ diagnostic plot.

Table 2 lists the redshifts of our IFRSs. In the SXDF, IFRSs are found to be distributed over $z = 1.68$–4.32, while in the VLA-VVDS field, a lower limit of $z > 2.0$ is placed for all but one (at $z = 2.45$) IFRSs (see Table 2). We note that the redshift estimates of our sample IFRSs in the two fields are consistent with previous studies that suggest that IFRSs are high-redshift objects (see Garn & Alexander 2008; Huynh et al. 2010; Collier et al. 2014). However, given the faintness of IFRSs in the optical and IR bands, most previous attempts were limited to obtaining the lower limit on redshifts based on SED modelling (see Garn & Alexander 2008; Huynh et al. 2010; Herzog et al. 2014, 2015b). Therefore, we emphasize that the deep optical and IR data available in the SXDF allow us to obtain the spectroscopic or photometric redshifts of all IFRSs in this field. In fact, our study of IFRSs in the SXDF provides the first instance where all IFRSs found in a deep field have redshift estimates.

However, unlike in the SXDF, the optical and IR data in the VLA–VVDS field are relatively less deep (see Table 1), which, in turn, causes the lack of redshift measurements of our IFRSs. Indeed, the lack of redshift estimates for IFRSs is a very common issue. For instance, in a large sample of 1317 relatively bright IFRSs, Collier et al. (2014) obtained spectroscopic redshifts of only 19 IFRSs from the SDSS DR9, and all but one of these IFRSs are found be quasars

located at $2 < z < 2.99$. Using VLT observations, Herzog et al. (2014) attempted to estimate the redshifts of four IFRSs that are relatively bright in the optical ($m_r \sim 22$–24; Vega magnitude) in the ATLAS field and found redshifts for the three brightest IFRSs at 1.84, 2.13 and 2.76. Therefore, in comparison to the previous studies that could find IFRSs at $z \leq 2.99$, our study reveals, for the first time, IFRSs at the highest redshift (i.e. $z > 3.0$). We also note that the deep data in the SXDF allow us to find redshifts for IFRSs at the faintest flux levels (see Section 5).

5 COMPARISON OF OUR IFRSS WITH PREVIOUS IFRS SAMPLES

In order to highlight the new parameter space investigated in our study, we compare our IFRSs with previous IFRS samples using $S_{3.6\,\mu m}$ versus $S_{1.4\,GHz}$ and $S_{3.6\,\mu m}$ versus z plots (see Fig. 4). Also, in Table 3, we list details (i.e. field, survey area, sensitivity in the radio and IR surveys, number of IFRSs, 1.4-GHz and 3.6-μm flux ranges with their median values, number of IFRSs with redshift estimates and redshift ranges with their median values) of various IFRS samples. We note that all IFRS samples (i.e. our IFRSs, IFRSs in other deep fields and the bright IFRS sample) follow the same selection criteria as proposed by Zinn et al. (2011). From Fig. 4 (left panel) and Table 3, it is obvious that, in comparison to the previous IFRS samples, our IFRS sample reaches down to the faintest flux level in the radio ($S_{1.4\,GHz} = 0.7$ mJy) and 3.6-μm ($S_{3.6\,\mu m} < 1.3$ μJy) bands because of the depths of our data. Our 3.6-μm SpUDS data ($5\sigma = 1.3$ μJy beam^{-1}) in the SXDF are the second deepest *Spitzer* survey after the S-COSMOS ($5\sigma = 1.0$ μJy beam^{-1}). In the radio band also, our data are the second deepest data ($5\sigma = 80$–100 μJy beam^{-1}) after the radio data in the COSMOS field. The relatively higher flux densities of IFRSs in the COSMOS and in other deep fields may also be due to slightly higher cut-off (S/N $\geq 10\sigma$) imposed during the IFRS sample selection (see Zinn et al. 2011). In comparison to the bright IFRS sample reported in Collier et al. (2014), our IFRS sample includes nearly one order of magnitude fainter sources in both radio and 3.6-μm bands (see Table 3).

Fig. 4 (right panel) shows $S_{3.6\,\mu m}$ versus z for IFRSs and HzRGs taken from different samples. In the literature, this diagram has been used to understand the nature of HzRGs and IFRSs (see Jarvis et al. 2009; Norris et al. 2011b; Collier et al. 2014). In the $S_{3.6\,\mu m}$

Table 3. Comparison of various IFRS samples. Only confirmed IFRSs in the SXDF and VLA-VVDS are considered. The details on the IFRS samples in deep fields (CDF-S, ELAIS-S1, xFLS and COSMOS) are based on Zinn et al. (2011). N_{IFRS} denotes the number of IFRSs, $N_{det,3.6\,\mu m}$ the number of IFRSs with detected 3.6-μm counterparts and N_z the number of IFRSs with redshift estimates. References are: 1, this work; 2, Norris et al. (2006); 3, Middelberg et al. (2008); 4, Garn & Alexander (2008); 5, Zinn et al. (2011); 6, Collier et al. (2014).

Ref.	Field	Area (deg²)	$S_{1.4\,GHz}$ limit 5σ (μJy beam⁻¹)	$S_{3.6\,\mu m}$ limit 5σ (μJy beam⁻¹)	N_{IFRS}	$S_{1.4\,GHz}$ range (mJy)	$N_{det,3.6\,\mu m}$	$S_{3.6\,\mu m}$ range (μJy)	N_z	z range
1	SXDF	0.8	100[a]	1.3[b]	6	0.7–50.8 (16.0)	5	<1.3–29.8 (13.9)	6	1.75–3.6 (2.92)
1	VLA-VVDS	1.0	80[c]	2.0[d]	3	1.4–19.0 (8.6)	1	<2.0 (< 2.0)	1	2.45–>2.0 (> 2.0)
2	CDF-S	3.7	186	3.1[e]	14	3.7–42.5 (11.9)	11	<3.0–29.3 (11.1)	3	1.84–2.76 (2.13)
3	ELAIS-S1	3.6	160	3.1[e]	15	1.7–33.6 (15.2)	9	<3.0–28.0 (3.0)	–	–
4	xFLS	3.1	105[f]	9.0[g]	13	1.4–35.8 (4.1)	6	<3.0–22.2 (< 7.3)	–	–
5	COSMOS	1.1	65[h]	1.0[i]	13	4.1–25.3 (7.0)	13	4.3–28.8 (13.0)	–	–
6	URC-SDSS	11000	1000	80[j]	1317	7.9–793.4 (25.5)	1317	10.3–30.0 (25.94)	19	0.5–2.99 (2.38)

Notes. [a]VLA BnC (Simpson et al. 2006). [b]SpUDS (Dunlop et al. 2007). [c]VLA B (Bondi et al. 2003). [d]SERVS (Mauduit et al. 2012). [e]SWIRE (Lonsdale et al. 2003). [f]VLA B (Condon et al. 2003). [g]*Spitzer* (Lacy et al. 2005). [h]VLA AnC (Schinnerer et al. 2007). [i]S-COSMOS (Sanders et al. 2007). [j]*WISE* (Wright et al. 2010).

versus z diagram, we show the positions of our IFRSs, the IFRSs from previous samples (Collier et al. 2014; Herzog et al. 2014), less powerful HzRGs ($L_{1.4\,GHz} > 10^{24}$ W Hz⁻¹; Singh et al. 2014) and powerful HzRGs ($L_{3\,GHz} > 10^{26}$ W Hz⁻¹; Seymour et al. 2007). For HzRGs, we consider only sources with $z \geq 1.0$. From the $S_{3.6\,\mu m}$ versus z plot (Fig. 4; right panel), it is apparent that our study finds redshifts of IFRSs at much fainter flux limits (i.e. $S_{3.6\,\mu m} < 1.3$ μJy), in comparison to previous studies where redshift measurements were limited to relatively bright IFRSs (i.e. $S_{3.6\,\mu m} \sim 20$–30 μJy). In fact, we find the first spectroscopic redshift of an IFRS at $S_{3.6\,\mu m} < 15$ μJy, while previous studies provided spectroscopic redshifts of IFRSs at $S_{3.6\,\mu m} = 17$–30 μJy (see Herzog et al. 2014; Collier et al. 2014). Also, we obtain the first photometric redshift of an IFRS at $S_{3.6\,\mu m} < 1.3$ μJy (see Table 2).

Furthermore, the availability of redshift estimates for faint IFRSs in our sample allows us to compare the nature of faint and bright IFRSs. In the $S_{3.6\,\mu m}$ versus z diagram, we find that powerful HzRGs exhibit a trend of decreasing 3.6-μm flux with the increase in redshift. Also, the inclusion of less powerful HzRGs shows a similar trend but with a larger scatter. We note that all confirmed IFRSs, in our sample as well as in the previous samples, follow the trend shown by HzRGs, which can be understood as IFRSs are radioloud AGNs (see Section 6). The candidate IFRSs at $z > 2$, with no detected 3.6-μm counterparts, tend to deviate in the $S_{3.6\,\mu m}$ versus z plot, as these are possibly weaker radio AGNs. In general, powerful HzRGs are found to be hosted in massive galaxies that are bright in the 3.6-μm band, in which stellar emission dominates (Jarvis et al. 2001; Seymour et al. 2007). Therefore, relatively less powerful HzRGs at similar redshifts are expected to be relatively fainter in the 3.6-μm band, which is apparent from the $S_{3.6\,\mu m}$–z plot. To probe the correlation between faint and bright IFRSs, it might be useful to derive a correlation equation for IFRSs in the $S_{3.6\,\mu m}$–z plot. However, we caution that the redshift estimates are available only for relatively bright sources spanning a small range of $S_{3.6\,\mu m}$ (i.e. 20–30 μJy; Herzog et al. 2014; Collier et al. 2014) along with a few IFRSs at fainter flux and higher-redshift regime. Hence, the $S_{3.6\,\mu m}$–z correlation equation derived from the present

data points would be biased and non-representative of the full IFRS population. Therefore, we present only a qualitative comparison between IFRSs and HzRGs in the $S_{3.6\,\mu m}$–z plot.

6 RADIO PROPERTIES OF OUR IFRSS

In this section, we discuss the radio properties of our IFRSs.

6.1 1.4-GHz and 3.6-μm flux densities

The 1.4-GHz radio flux densities of IFRSs in our sample are distributed over 0.1–50.8 mJy with a median of 0.7 mJy (see Table 2 and Fig. 4). The confirmed IFRSs are distributed over $S_{1.4\,GHz}$ = 0.68–50.8 mJy with a median of 8.9 mJy, while the candidate IFRSs span $S_{1.4\,GHz}$ = 0.109–1.58 mJy with a median of 0.238 mJy. Therefore, at radio wavelengths, the confirmed IFRSs in our sample are systematically brighter than the candidate IFRSs. The 3.6-μm flux densities of confirmed IFRSs range from <1.3 to 29.8 μJy with a median of 3.2 μJy, while all the candidate IFRSs show no detected 3.6-μm counterparts at the 5σ level. The candidate IFRSs can only be true IFRSs if their 3.6-μm flux densities are, on average, 1.2–6.25 times lower than their upper limits. The visual inspection of the 3.6-μm image cut-outs shows no detection even at the faintest level. Thus, if we assume an upper limit of 3.6-μm flux at the 1σ level (0.26 μJy in the SpUDS and 0.4 μJy in the SERVS), then all but two candidate IFRSs will be confirmed IFRSs. We perform the median stacking of 3.6-μm SERVS and SpUDS image cut-outs at the radio positions of 13 IFRSs with no detected 3.6-μm counterparts, and we do not obtain any detection in the stacked image with the average rms noise of ∼0.09 μJy beam⁻¹. Therefore, on average, the 3.6-μm flux of our IFRSs with undetected 3.6-μm counterparts is < 0.27 μJy (assuming 3σ of the median stacked image), and thus suggesting that most, if not all, candidate IFRSs are likely to be true IFRSs. Also, the candidate IFRSs with relatively higher ratio of radio-to-IR flux (i.e. $S_{1.4\,GHz}/S_{3.6\,\mu m} > 350$) are brighter in the radio and have higher probability of being true IFRSs. The candidate IFRSs with lower ratio

of radio-to-IR flux can represent an extreme IFRS population, which contains either powerful radio sources at much higher redshifts ($z \geq 5.0$) or less powerful radio sources at moderate redshifts ($z \sim 2.0$–3.0). We note that the IFRSs in our sample are distributed over a wide range of radio flux densities, IR flux densities and the ratios of radio-to-IR, which is consistent with the previous IFRS samples. For example, Zinn et al. (2011) presented a sample of 55 IFRSs (with S/N cut-off $\geq 13\sigma$) from four deep fields (i.e. ELAIS-S1, CDFS, xFLS and COSMOS) and found them to be distributed over $S_{1.4\,\mathrm{GHz}} \sim 1.14$–42.2 mJy with a median of 7.8 mJy. For our IFRS sample, we use a lower value of S/N cut-off (i.e. 8σ), which allows us to find IFRSs in the sub-mJy regime.

6.2 Radio morphologies, sizes and luminosities

The radio morphologies of IFRSs can provide clues for understanding their nature. Therefore, we investigate radio morphologies of our IFRSs using both 1.4-GHz and 325-MHz observations. The morphologies at two frequencies can be used in a complementary fashion as 1.4-GHz VLA observations are more useful in resolving the structures because of relatively higher resolution, while low-frequency 325-MHz observations can be more effective in detecting diffuse relic emission. In Fig. A1, we show 1.4-GHz radio contours of IFRSs overlaid on to their 3.6-μm images. Using 1.4-GHz observations, we find that 14/19 IFRSs in our sample are unresolved point sources, while five IFRSs show extended radio emission. There are three confirmed IFRSs (J021839−044149, J022420−042544 and J022526−043454) and one candidate IFRS (J022631−042453) that show distinct double-lobe radio morphology, thus confirming them to be typical radio galaxies. A candidate IFRS J022631−042453 ($S_{1.4\,\mathrm{GHz}}/S_{3.6\,\mu\mathrm{m}} > 350$) also shows extended morphology with a marginally resolved double-lobe-like structure. Thus, with the 1.4-GHz radio morphology itself, it is evident that at least a fraction of IFRSs are radio galaxies at higher redshifts. The 325-MHz radio morphologies seem less informative because of their relatively lower resolution (i.e. 9.0 arcsec) and lower sensitivity ($5\sigma \simeq 750\,\mu\mathrm{Jy\ beam}^{-1}$). At 325 MHz, some of the IFRSs with double-lobe morphologies, seen in 1.4 GHz, appear as unresolved point sources (i.e. J021839−044149), blended with a nearby source (i.e. J021740−045157) and undetected because of their inverted/flat radio spectra (i.e. J021859−050837 and J021801−044200).

We try to constrain the 1.4-GHz radio sizes of our IFRSs, irrespective of their apparent radio morphology. For extended sources, we obtain their projected linear sizes by measuring the distance between the two extremes along the direction of extension. For unresolved point sources, we fit them with a single Gaussian component using the JMFIT task in the Astronomical Image Processing System (AIPS[1]). For unresolved sources, we consider the upper limit on their radio size as $\sqrt{(\mathrm{max}) \times (\mathrm{min})}$, where 'max' and 'min' are the upper limits on the major and minor axes, respectively, of the deconvolved Gaussian fit obtained from JMFIT. If the upper limit on the deconvolved minor axis is '0', we set the upper limit on the minor axis equal to the upper limit on the major axis.

It is evident that all the unresolved sources are compact with the upper limit on their sizes ranging from 10 to 50 kpc, while the linear projected size of extended sources ranges from 96 to 330 kpc (see Table 2 and Fig. 5). Among the nine confirmed IFRSs,
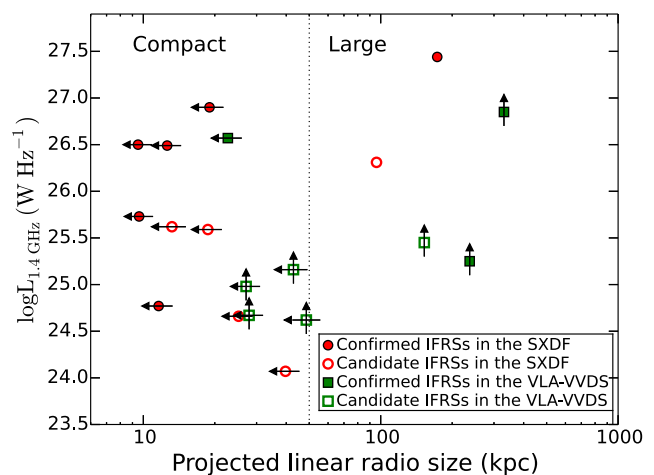
Figure 5. Radio luminosity versus projected linear radio size plot for our IFRSs. The vertical dotted line separates compact and large, extended sources.

six are compact sources with their radio sizes ≤ 23 kpc and three are extended double-lobe sources with the projected linear sizes of 173, 237 and 331 kpc. The double-lobe morphology of some of our IFRSs is consistent with the previous hypotheses of IFRSs being radio galaxies at high-z. The typical radio size of an evolved radio galaxy is ~ 100 kpc or larger (Pentericci et al. 2000), and therefore our IFRSs, which have smaller radio sizes, might be young radio galaxies. Garn & Alexander (2008) reported the upper limits on the radio sizes of IFRSs with unresolved morphologies to be ≤ 20 kpc, which is similar to our results. VLBI observations of relatively bright IFRSs revealed only a compact radio core with the upper limit on their radio sizes limited only to a few hundred parsec (Norris et al. 2007; Middelberg et al. 2008; Herzog et al. 2015a). We also note that the resolution of VLA observations (i.e. 6.0 arcsec) used in our study is better than the ATLAS observations (i.e. 11.0×5.0 arcsec^2; Norris et al. 2006), and therefore we are likely to find more double-lobe radio sources.

The radio luminosities of IFRSs can also be used to characterize their nature. We estimate 1.4-GHz rest-frame radio luminosities of our IFRSs that are K-corrected by assuming a power-law radio spectrum ($S_\nu \propto \nu^{-\alpha}$) and the spectral index measured between 325 MHz and 1.4 GHz ($\alpha_{325\mathrm{MHz}}^{1.4\,\mathrm{GHz}}$). Thus, the radio luminosity of an IFRS at redshift z and luminosity-distance d_L is given by $L_\nu = 4\pi d_L^2 S_\nu (1 + z)^{-(1+\alpha)}$. We find that the 1.4-GHz radio luminosities of our IFRSs are distributed over 1.2×10^{24} to 2.7×10^{27} W Hz^{-1} with a median of 3.8×10^{25} W Hz^{-1} (see Table 2). For confirmed IFRSs, the 1.4-GHz radio luminosities range from 5.8×10^{24} to 2.7×10^{27} W Hz^{-1} with a median of 3.2×10^{26} W Hz^{-1}, while the radio luminosities of candidate IFRSs span 1.2×10^{24} to 2.0×10^{26} W Hz^{-1} with a median of 1.2×10^{25} W Hz^{-1}. Given the high 1.4-GHz radio luminosities, all our IFRSs can only be AGNs as galaxies with $L_{1.4\,\mathrm{GHz}} \geq 10^{24}$ W Hz^{-1} cannot be powered by star formation or starburst alone (Afonso et al. 2005; Mauch & Sadler 2007). Therefore, the high radio luminosities of our IFRSs suggest that they are radio-loud AGNs in which radio emission is due to non-thermal synchrotron radiation from relativistic jets (Rafter, Crenshaw & Wiita 2009). The radio luminosities of our IFRSs straddle across the radio luminosity break between Fanaroff–Riley type I/II (FR I/FR II) radio galaxies (i.e. $L_{1.4\,\mathrm{GHz}} = 10^{25.6}$ W Hz^{-1} derived from $L_{178\mathrm{MHz}} = 10^{26}$ W Hz^{-1}, assuming a typical spectral index of -0.7; Fanaroff & Riley 1974). Thus, a fraction of our IFRSs with

---
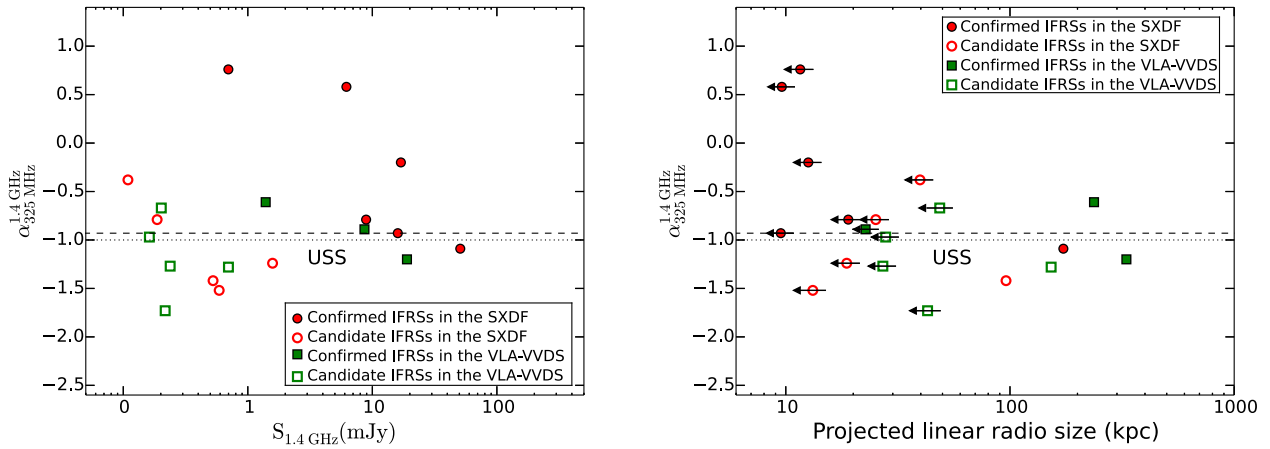
Figure 6. Left panel: $\alpha_{325\text{MHz}}^{1.4\,\text{GHz}}$ versus $S_{1.4\,\text{GHz}}$ plot. Right panel: $\alpha_{325\text{MHz}}^{1.4\,\text{GHz}}$ versus radio size plot. Error bars are small and are of the order of the sizes of symbols. The horizontal dashed and dotted lines represent the median value ($\alpha_{325\text{MHz}}^{1.4\,\text{GHz}} = -0.93$) of the spectral index distribution and the USS limit ($\alpha_{325\text{MHz}}^{1.4\,\text{GHz}} = -1.0$), respectively.

$L_{1.4\,\text{GHz}} \geq 10^{25.6}$ W Hz^{-1} are powerful FR II radio galaxies. Furthermore, the FR I/FR II break radio luminosity is a function of optical luminosity of the host galaxy (Ghisellini & Celotti 2001), and therefore optically faint IFRSs (i.e. $m_r \geq 25$ at $z \geq 2.0$ for IFRSs corresponding to $M_r > -21$) with lower radio luminosities ($L_{1.4\,\text{GHz}} \sim 10^{24}$–$10^{25}$ W Hz^{-1}) can also be of FR II type radio galaxies. Indeed, the double-lobe radio morphologies seen in some of our IFRSs suggest that they are FR II-like radio galaxies. In fact, Garn & Alexander (2008) have shown that IFRSs can be modelled as less luminous FR II radio galaxies at high redshifts.

To understand the nature of our IFRSs, we also plot the radio size versus radio luminosity (see Fig. 5). As mentioned earlier, IFRSs can be grouped into two categories: compact sources with the upper limit on their radio sizes ranging from ≤ 10 to ≤ 50 kpc and extended sources with the linear projected size ranging from 96 to 330 kpc. From Fig. 5, it is evident that all the extended sources are radio powerful with $L_{1.4\,\text{GHz}} = 1.8 \times 10^{25}$ to 2.7×10^{27} W Hz^{-1}, while the compact sources are distributed across moderate to high radio luminosities ($L_{1.4\,\text{GHz}} = 1.2 \times 10^{24}$ to 7.9×10^{26} W Hz^{-1}). This suggests that the IFRS population consists of powerful double-lobe radio galaxies as well as less powerful compact radio-loud AGNs (possibly young radio galaxies).

6.3 Radio spectra

To examine the nature of the radio spectra of our IFRSs, we measure the spectral index between 1.4 GHz and 325 MHz (see Table 2). In the SXDF, we are limited to a two-point (1.4 GHz–325 MHz) spectral index, while in the VLA-VVDS we obtain a three-point (1.4 GHz–610 MHz–325 MHz) spectral index using the least-squares fit method. The resolutions of 1.4-GHz VLA, 610-MHz GMRT and 325-MHz GMRT observations are not too different i.e. 6.0, 6.0 and 9.0 arcsec, respectively), and therefore our spectral index estimates are unlikely to be affected by the resolution bias. For our full sample, the radio spectral indices span +0.76 to −1.73 with a median of −0.93 (see Fig. 6). The radio spectral indices ($\alpha_{325\text{MHz}}^{1.4\,\text{GHz}}$) of our confirmed IFRSs range from +0.76 to −1.2 with a median of −0.79, while the spectral indices of the candidate IFRSs are distributed over −0.38 to −1.73 with a median of −1.24. From the $S_{1.4\,\text{GHz}}$ versus $\alpha_{325\text{MHz}}^{1.4\,\text{GHz}}$ plot (see Fig. 6, left panel), it is evident that the candidate IFRSs are not only systematically fainter but also ex-

hibit systematically steeper spectra. Six out of 11 candidate IFRSs can be classified as USS radio sources (i.e. $\alpha_{325\text{MHz}}^{1.4\,\text{GHz}} \geq -1.0$), while only two out of nine confirmed IFRSs fall into the USS category. In general, USS sources are believed to be high-z sources because of the z–α correlation (Miley & De Breuck 2008; Ker et al. 2012). In fact, the z–α correlation is used to search for high-z radio galaxies (see Ishwara-Chandra et al. 2010; Singh et al. 2014). Therefore, given the z–α correlation, all the candidate IFRSs with steep radio spectra are likely to be high-z sources. Indeed, all the USS candidate IFRSs in the SXDF have redshifts over 1.68–4.32. Therefore, the assumption of candidate IFRSs with no IR counterparts being at $z \geq 2.0$ (see Section 4) is further supported by the fact that they are USS sources. However, we caution that all USS sources are not guaranteed to be high-z sources, and vice versa (Afonso et al. 2011).

Apart from the IFRSs with steep spectra, there are two confirmed IFRSs in the SXDF with positive spectral indices ($\alpha_{325\text{MHz}}^{1.4\,\text{GHz}} = 0.58$ and 0.76) and these might possibly be gigahertz peaked spectrum (GPS) sources. The GPS radio sources show a turnover in their radio spectra at 500 MHz or higher frequencies in the rest frame (Fanti 2009). Both IFRSs with positive spectral indices between 325 MHz and 1.4 GHz can have turnover frequency at ≥ 1.4 GHz in the observed frame, which corresponds to ≥ 357 MHz and ≥ 304 MHz in their respective rest frames at redshifts 2.92 and 3.6, respectively. Moreover, we need high-frequency (≥ 1.4 GHz) radio observations to confirm if these IFRSs are GPS sources.

It is interesting to note that the radio spectral indices of both the confirmed and candidate IFRSs are widely distributed and deviate from the typical value of spectral index ($\alpha \sim -0.7$) for the general radio population (see Fig. 6). This suggests that our IFRSs are unlikely to consist of SFGs and/or radio-quiet AGNs. The distribution of radio spectral indices of our sample IFRSs is in agreement with the results from previous studies (Middelberg et al. 2011; Herzog et al. 2016), which found IFRSs exhibiting primarily steep spectra. For instance, Middelberg et al. (2011) studied the radio spectra over 1.4 GHz to 8.4 GHz for 18 IFRSs and reported that the IFRS spectra at higher frequencies are remarkably steep with a median of $\alpha_{1.4\,\text{GHz}}^{2.4\,\text{GHz}} \sim -1.4$, and lack sources with spectral indices ($\alpha_{1.4\,\text{GHz}}^{2.4\,\text{GHz}}$) higher than −0.7. The steeper high-frequency radio spectra of IFRSs reported in Middelberg et al. (2011), in comparison with the relatively less steep low-frequency radio spectra of our IFRSs, can be explained if IFRS spectra steepen towards higher frequencies.

Table 4. Multiwavelength counterparts of our IFRSs. In the VLA-VVDS field, the *r*-band magnitudes are from the CFHTLS-D1. The *K*-band magnitudes in the SXDF are based on the UDS DR 11 and the lower limits are set equal to the median depth (5σ) of the UDS DR 11. Two IFRSs in the SXDF lie outside the UDS footprint and the lower limits ($m_K > 15.85$) are based on the 2MASS. The 24-μm counterparts are searched from the SpUDS and SWIRE surveys, while 250-μm fluxes are based on the HerMES level 4 data. The X-ray counterparts are searched from the SXDS and XMDS surveys (see Table 1).

RA (h m s)	Dec. (° ′ ″)	m_r	m_K	$S_{24\,\mu m}$ (mJy)	$m_r - m_{24\,\mu m}$	$q_{24\,\mu m}$	$S_{250\,\mu m}$ (mJy)	$S_{2.0-10\mathrm{keV}}$ (erg s^{-1} cm^{-2})
SXDF								
02 18 39.55	−04 41 49.4	23.45 ± 0.01	18.98 ± 0.01	0.306 ± 0.023	5.76	−2.22	–	–
02 17 52.12	−05 05 22.4	26.87 ± 0.10	21.34 ± 0.03	<0.1	<7.97	<−1.79	–	$6.38 \pm 2.06 \times 10^{-15}$
02 18 53.63	−04 47 35.6	24.42 ± 0.02	19.26 ± 0.01	0.671 ± 0.026	7.57	−1.40	13.2 ± 1.3	
02 18 51.38	−05 09 01.6	23.97 ± 0.01	18.65 ± 0.01	<0.1	<5.07	<−2.20	–	
02 18 03.41	−05 38 25.5	24.55 ± 0.02	>15.85	<0.1	<5.65	<−1.95		
02 18 38.24	−05 34 44.2	26.69 ± 0.10	>15.85	<0.45	<9.45	<−0.55		
02 17 40.69	−04 51 57.3	25.53 ± 0.03	22.32 ± 0.06	<0.45	<8.26	<−0.07	–	–
02 17 45.84	−05 00 56.4	>27.7	>25.3	<0.1	<8.80	<−0.77	–	–
02 18 01.23	−04 42 00.8	26.36 ± 0.06	22.10 ± 0.07	<0.1	<7.46	<−0.04	–	–
02 18 30.13	−05 17 17.4	28.64 ± 0.15	>25.3	<0.1	<9.74	<−0.27	–	–
02 18 59.19	−05 08 37.8	>27.7	>25.3	<0.1	<8.8	<−0.84	–	–
VLA-VVDS								
02 27 48.26	−04 19 05.3	26.18 ± 0.18	>23.5	<0.45	<8.91	<0.44	–	–
02 25 02.13	−04 40 26.9	25.61 ± 0.10	>23.5	<0.45	<8.34	<0.35	–	–
02 26 58.10	−04 18 14.9	24.61 ± 0.04	>23.5	<0.45	<7.34	<0.32	–	–
02 27 09.90	−04 23 44.8	26.25 ± 0.21	>23.5	<0.45	<8.98	<0.27	–	–
02 26 31.12	−04 24 53.3	26.48 ± 0.24	>23.5	<0.45	<9.21	<0.19	–	–
02 25 26.14	−04 34 54.4	26.02 ± 0.14	>23.5	<0.45	<8.57	<−0.49	–	–
02 26 09.09	−04 33 34.7	25.04 ± 0.25	21.80 ± 0.09	0.347 ± 0.022	7.49	−1.39	–	–
02 24 20.96	−04 25 44.6	26.86 ± 0.32	>23.5	<0.45	<9.59	<−1.62	–	–

Indeed, based on the comparison of the resolution-matched spectral indices between 1.4 and 2.4 GHz ($\alpha_{1.4\,\mathrm{GHz}}^{2.4\,\mathrm{GHz}}$) and between 4.8 and 8.6 GHz ($\alpha_{4.8\,\mathrm{GHz}}^{8.6\,\mathrm{GHz}}$), Middelberg et al. (2011) reported that the radio spectra of IFRSs generally steepen towards higher frequencies. However, Herzog et al. (2016) reported that the radio spectra of relatively bright IFRSs can be characterized by a single power law over a large frequency range of 150 MHz–34 GHz, and, on average, IFRSs show steep spectra ($\alpha < -0.8$), but also include GPS sources exhibiting turnover at ∼1 GHz.

Fig. 6 (right panel) shows that the powerful extended sources in our sample exhibit steep spectral indices, which is one of the characteristic features of HzRGs, while the compact sources in our sample are widely distributed in spectral indices and include steep, flat and inverted spectra that can be characterized as compact steep spectrum (CSS) and GPS sources. Both CSS and GPS sources are believed to represent the initial phase of the evolutionary path of radio galaxies (Tinti & de Zotti 2006; Fanti 2009). Thus, we find that our IFRSs constitute a diverse population of radio-loud AGNs widely distributed over radio luminosities, radio sizes and spectral indices. Therefore, it seems likely that our IFRSs are HzRGs in different evolutionary phases.

7 MULTIWAVELENGTH COUNTERPARTS OF OUR IFRSS

To understand the nature of our IFRSs, we also attempt to find their multiwavelength (i.e. optical, NIR, MIR, FIR and X-ray) counterparts using the existing deep data in both fields. The counterparts of our IFRSs in different bands are searched by considering the closest match within a circle centred at the radio position and having radius equal to the one-third of the larger beam size in the two cross-matching bands. The search radii used to find counterparts in different bands are similar to those derived from the cross-matching of large samples at different wavelengths (e.g. Ivison et al. 2007).

We note that our IFRSs are the subset of radio sources detected in the 1.4-GHz VLA surveys in both fields. The optical counterparts for all 1.4-GHz radio sources are searched using the likelihood ratio method, and only reliable optical counterparts are considered; that is, there is ≥90 per cent probability that the identified optical counterpart is associated with the radio source (see Simpson et al. 2006; McAlpine et al. 2012). In order to estimate the fraction of chance matches, we shifted the positions of radio sources by 30–45 arcsec in random directions, and thereafter cross-matched the radio and optical catalogues using the previously opted search radius. The cross-matching of radio sources with shifted positions and optical sources resulted in only 2–4 per cent of the total radio sources (see Singh et al. 2014). Therefore, the probability of an optical counterpart being merely a chance match is limited only to a few per cent. The lower surface source density in other bands (i.e. NIR, MIR, FIR and X-ray) results in an even lower fraction of chance matches.

Table 4 lists the magnitudes/fluxes of the multiwavelength counterparts of our IFRSs. We note that the detection rate is highest in the optical band in which all but two IFRSs show counterparts. The *r*-band magnitudes of our sample IFRSs are widely distributed and range from 23.5 to 28.6 with a median of 26. The deep optical data available in both fields allow us to obtain a much higher detection rate than that reported in previous studies (e.g. Garn & Alexander 2008; Collier et al. 2014). We note that the radio-bright IFRSs are also bright in the optical and NIR bands. Moreover, both radio-bright and radio-faint IFRSs are present at similar redshifts, suggesting that the IFRSs constitute a diverse population.

In the 24-μm MIR band, only three IFRSs show counterparts and for the remaining sources we put an upper limit based on the sensitivity limit of SpUDS ($5\sigma = 0.1$ mJy beam^{-1}) and SWIRE ($5\sigma = 0.45$ mJy beam^{-1}) surveys. To obtain further insight into the nature of our IFRSs, we estimate the ratio of 24-μm MIR to 1.4-GHz radio flux densities, which is defined as $q_{24\,\mu m} = \log_{10}(S_{24\,\mu m}/S_{1.4\,\mathrm{GHz}})$. The $q_{24\,\mu m}$ parameter is conventionally used to segregate the
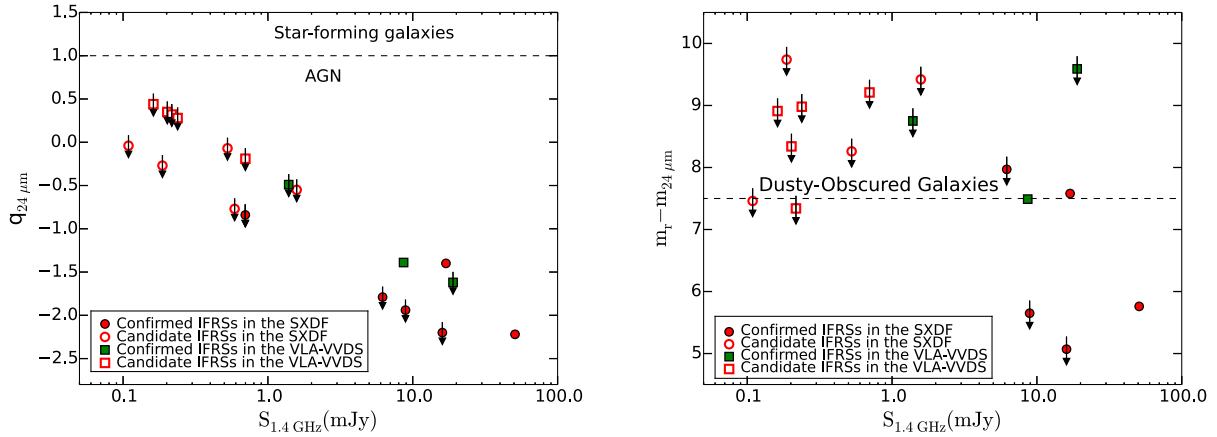
Figure 7. Left panel: $q_{24} = \log(S_{24\,\mu m}/S_{1.4\,GHz})$ versus $S_{1.4\,GHz}$ plot. Right panel: optical to 24-μm colour (m_r–$m_{24\,\mu m}$) versus $S_{1.4\,GHz}$ plot.

populations of AGNs and SFGs, because SFGs exhibit tight correlation between MIR and radio emission, while AGNs tend to deviate as a result of their radio excess (Appleton et al. 2004). We find that $q_{24\,\mu m}$ values of our IFRSs are in the range of ≤ 0.44 to -2.22 and show a large radio excess from the typical value of $q_{24\,\mu m} \simeq 1.0$ for SFGs, thus reinforcing the conclusion that IFRSs belong to the AGN population. Given the non-detection of 24-μm counterparts for most of our IFRSs, in particular in the radio-faint regime, it is unclear if $q_{24\,\mu m}$ values for radio-faint and radio-bright IFRSs are similar. The confirmed IFRSs clearly stand out with much lower values/limits of $q_{24\,\mu m}$ than that for candidate IFRSs (see Fig. 7, left panel).

We also investigate the optical-to-MIR colours of our sample sources to examine if our IFRSs are hosted in dust-obscured galaxies (DOGs). The DOGs at higher redshifts are faint in the UV and optical bands but become relatively bright in the MIR and FIR bands. In the literature, DOGs have been identified with colour cut of m_r–[24] ≥ 7.5 (AB mag) and $S_{24\,\mu m} > 100\,\mu$Jy (see Calanog et al. 2013). We obtain the optical-to-MIR colours (m_r–[24]) for our sample sources, and we obtain the lower limits on the colours for sources that do not show detected counterparts at 24 μm. Using the optical-to-MIR colours (m_r–[24]) we find that two of three IFRSs that show 24-μm counterparts can be classified as DOGs (see Table 4). From the radio flux density versus optical-to-MIR colour plot (Fig. 7, right panel) it is evident that a significant fraction of our IFRSs can belong to DOGs even if their 24-μm counterparts are one to two orders of magnitude fainter than the SpUDS and SWIRE sensitivity limits at 5σ. However, because of the lack of detected counterparts in the 24-μm band for the majority of IFRSs, we only have upper limits on the optical-to-MIR colours (m_r–[24]), which prevents us from obtaining the exact fraction of IFRSs hosted in DOGs and the variation of optical-to-MIR colour across the redshift. We perform image stacking to obtaint the average 24-μm flux of the IFRS population that remained undetected in the 24-μm *Spitzer* surveys (SpUDS and SWIRE). The stacking method involves making the 24-μm image cut-outs of 60×60 arcsec^2 centred at the radio positions of IFRSs and then obtaining a stacked image by combining all the image cut-outs on a pixel-by-pixel basis. We prefer to take the median rather than the mean, which can be affected by the presence of extreme outliers. The flux density is obtained from the value of the central pixel in the stacked image. For all our 16 IFRSs with no detected 24-μm counterparts, we stack 24-μm image cut-outs and find that the median stacked image does not show any detection with the

rms noise of $\simeq 0.014\,\mu$Jy beam^{-1}. The non-detection in the stacked 24-μm image suggests that a significant fraction of IFRSs are fainter than the typical DOGs ($S_{24\mu m} > 100\,\mu$Jy).

Because dusty galaxies are more probably detected in the FIR bands, we also search for the FIR counterparts of our IFRSs using the HerMES data. We find that only one IFRS (i.e. J021853−044735) is detected in the *Herschel*/SPIRE bands with fluxes of 13.2 ± 1.3, 13.9 ± 1.3 and 6.2 ± 1.9 mJy in the 250-, 350- and 500-μm bands, respectively. For all 18 IFRSs with no 250-μm counterparts, we obtain a median stacked image using a method similar to the one performed for the 24-μm band. We find that the stacked 250-μm HerMES image does not show any detection with the rms noise of $\simeq 0.52$ mJy beam^{-1}. The non-detections of all but one IFRSs in the *Herschel*/SPIRE bands might not be surprising because nearly half of the DOG population remained undetected in the 250-μm band at the 3σ level in the HerMES survey of the COSMOS deep field (see Calanog et al. 2013). As expected, the DOG population undetected at 250 μm is, on average, relatively less luminous in the IR and has higher dust temperature. The non-detection of most of our sample IFRSs in the FIR bands is consistent with previous studies. For example, Herzog et al. (2015b) found that all six IFRSs in their sample remained undetected in all five bands of *Herschel* (with stacking limits $\sigma = 0.74$, 2.68 and 3.45 mJy beam^{-1} at 100, 250 and 500 μm, respectively). By comparing the SED templates of different types of galaxies with the upper limits of fluxes at 3.6 μm, 24 μm and FIR bands Herzog et al. (2015b) concluded that the non-detections of radio-bright IFRSs (7–25 mJy) can only be explained if IFRSs are: (i) HzRGs at very high redshifts ($z \geq 10.5$); (ii) low-luminosity variants of HzRGs with additional dust obscuration at moderate redshifts; (iii) scaled or unscaled versions of Cygnus A at any redshift; (iv) scaled and dust-obscured radio-loud quasars or CSS sources. We further note that all our IFRSs are unlikely to be hosted in DOGs. For instance, Zinn et al. (2011) demonstrated that a fraction of IFRSs are possibly similar to 3C 48 placed at high redshifts and such IFRSs will fall below the detection limits of the SWIRE and the *Herschel* bands. We note that, based on the optical spectra, one of our IFRSs, J021839−044149, is classified as a narrow-line AGN, while two other IFRSs (i.e. J021853−044735 and J021803−053825) are also possible narrow-line AGNs (see Section 4).

We also search for the X-ray counterparts of our IFRSs using the deepest available X-ray surveys (i.e. SXDS and XMDS; see Table 1). Only one IFRS shows X-ray counterparts. IFRS

J021752−050522 is detected in the SXDS with the X-ray flux of $S_{0.5-2.0keV} \simeq 2.5 \pm 1.7 \times 10^{-16}$ erg s^{-1} cm^{-2} and $S_{2.0-10keV} \simeq 6.38 \pm 2.06 \times 10^{-15}$ erg s^{-1} cm^{-2}, where fluxes are estimated from the count rates assuming photon index (Γ) = 1.7 of the X-ray spectrum and conversion factors given in Ueda et al. (2008). The estimated X-ray luminosities in the soft and hard X-ray bands are $L_{0.5-2.0keV}$ = $1.87 \pm 1.27 \times 10^{43}$ erg s^{-1} and $L_{2.0-10keV} = 4.77 \pm 1.54 \times 10^{44}$ erg s^{-1}, respectively. The hard X-ray luminosity is similar to the X-ray bright quasars in the local Universe (Ballo et al. 2014). The non-detection of most of our sample IFRSs is consistent with previous studies (e.g. Zinn et al. 2011). For example, Huynh et al. (2010) used the *Chandra* 2Ms source catalogue and did not find the X-ray counterpart of any IFRS in the CDFS field. The non-detection of our IFRSs in the X-ray band further reinforces the notion that IFRSs are hosted in dusty galaxies and the X-ray emission is absorbed by the dust present in the host galaxy. In fact, it is proposed that IFRSs can be part of the missing population of Compton-thick AGNs predicted by the models of cosmic X-ray background emission (see Zinn et al. 2011).

8 SUMMARY AND CONCLUSIONS

In this paper, we identify and investigate the nature of IFRSs in the SXDF and VLA-VVDS fields using one of the deepest set of multiwavelength data currently available. The key results of our study are outlined below.

(i) With the selection criteria of $S_{1.4\,GHz}/S_{3.6\,\mu m} \geq 500$ and $S_{3.6\,\mu m} \leq 30\,\mu$Jy, we identify nine confirmed IFRSs (six in the SXDF and three in the VLA-VVDS) over 1.8 deg^2 in the two deep fields. We also identify ten candidate IFRSs (five in each of the two fields) with the selection criteria of a radio source with no 3.6-μm counterpart and the lower limit on $S_{1.4\,GHz}/S_{3.6\,\mu m}$ being less than 500. For candidate IFRSs, the visual inspection of 3.6-μm image cut-outs centred at the radio positions does not show any emission at the faintest level, thus inferring that they are true IFRSs if their 3.6-μm fluxes are below the 1σ detection limit.

(ii) The availability of deep radio ($S_{1.4\,GHz} \sim 80 - 100\,\mu$Jy beam^{-1} at 5$\sigma$), optical ($m_r \sim 26$–27.7 at 5$\sigma$) and NIR ($S_{3.6\,\mu m} \sim$ 1.3–2.0 μJy beam^{-1} at 5σ) data allows us to find IFRSs in the faintest flux regime. Also, in comparison with previous studies, we obtain the highest optical identification rate of IFRSs in the SXDF.

(iii) In the SXDF, all our IFRSs have spectroscopic or photometric redshifts that are distributed over $z = 1.68$–4.3. In the VLA-VVDS, all but one (at $z = 2.45$) IFRSs have only a lower limit $z > 2.0$, on their redshifts. We emphasize that by using deep multiwavelength data, our study reveals, for the first time, IFRSs at $z > 3.0$. Also, in comparison with previous studies, we find redshift estimates for IFRSs lying in the faintest 3.6-μm flux regime, for instance, an IFRS with spectroscopically measured redshift (z = 2.43) at $S_{3.6\,\mu m} = 13.6\,\mu$Jy and an IFRS with photometrically measured redshift ($z = 4.3$) at $S_{3.6\,\mu m} < 1.3\,\mu$Jy. Hitherto, all the previous attempts to measure the redshifts of IFRSs were limited to the relatively bright flux regime ($S_{3.6\,\mu m} = 20$–30 μJy) and at lower redshifts ($z \leq 2.99$).

(iv) The 1.4-GHz VLA radio images show that 14/19 sources in our sample are unresolved point sources, while five sources exhibit extended double-lobe morphology. Therefore, radio morphology itself reveals that at least a fraction of IFRSs are typical radio galaxies. The upper limits on the radio sizes of unresolved sources range from ≤ 10 to ≤ 50 kpc, while the projected linear radio sizes of the extended sources range from 96 to 330 kpc.

(v) The radio luminosity distribution of our IFRSs suggests that they are radio-loud AGNs with 1.4-GHz radio luminosity spanning from 1.2×10^{24} to 2.7×10^{27} W Hz^{-1} with a median of 3.8 $\times 10^{25}$ W Hz^{-1}. We note that high radio luminosities ($L_{1.4\,GHz} \geq 10^{24}$ W Hz^{-1}) cannot be powered by star formation or starburst alone. Also, all IFRSs with extended radio morphology show high radio luminosities ($L_{1.4\,GHz} \simeq 1.8 \times 10^{25}$ to 2.7×10^{27} W Hz^{-1}) that are typical of FR II radio galaxies. However, IFRSs that have compact radio morphologies are found to be widely distributed from moderate ($L_{1.4\,GHz} = 1.2 \times 10^{24}$ W Hz^{-1}) to high radio luminosity ($L_{1.4\,GHz} = 7.9 \times 10^{26}$ W Hz^{-1}).

(vi) The radio spectral indices measured between 1.4 GHz to 325 MHz ($\alpha_{325MHz}^{1.4MHz}$) for our IFRSs predominately show steep spectra with a median spectral index of -0.93, but our sample also contains sources with flat/inverted spectra. In comparison to the confirmed IFRSs (median $\alpha_{325MHz}^{1.4MHz} = -0.79$), the candidate IFRSs show systematically steeper spectra (median $\alpha_{325MHz}^{1.4MHz} = -1.24$) which suggests that they are at higher redshifts because of the z–α empirical correlation. The systematically steep radio spectra of our IFRSs also indicate that deeper low-frequency radio surveys can be more useful in unveiling IFRSs at higher redshifts.

(vii) Using the optical-to-MIR colours (m_r–$m_{24\,\mu m}$) we find that two out of three IFRSs detected in the 24-μm band are hosted in DOGs, while upper limits on the optical-to-MIR colours for the remaining IFRSs suggest that a large fraction of IFRSs are likely to be hosted in DOGs, even if their 24-μm fluxes are one to two orders of magnitude lower than their upper limits. The non-detection of all but one IFRSs in the deep X-ray surveys further supports the possibility of IFRSs being AGNs hosted in an obscured environment.

(viii) The IFRSs in our sample are widely distributed in a variety of parameters (i.e. optical magnitude, IR flux, radio flux density, radio size, radio power, radio spectral index and redshift). Therefore, it is likely that our IFRSs consist of a diverse population of radio-loud AGNs ranging from powerful radio galaxies to less powerful radio AGNs.

Our study, based on the two small-area deep fields, also acts as a test-bed to explore a large population of IFRSs by using data from upcoming large-area deep optical and IR surveys, such as the Large Synoptic Survey Telescope (LSST; Ivezic et al. 2008), the James Webb Space Telescope (JWST; Gardner et al. 2006) and the deep radio surveys from the upgraded GMRT (uGMRT), the Evolutionary Map of the Universe (EMU; Norris et al. 2011a) and the Square Kilometre Array (SKA; Dewdney et al. 2009).

and 610-MHz radio images of the VLA-VVDS field. We thank Chris Simpson for providing the 1.4-GHz VLA radio image of the SXDF field. This work is based on observations made with the *Spitzer Space Telescope*, which is operated by the Jet Propulsion Laboratory (JPL), California Institute of Technology (Caltech), under a contract with the National Aeronautics and Space Administration. This work used the CFHTLS data products, which are based on observations obtained with MegaPrime/MegaCam, a joint project of CFHT and CEA/DAPNIA, at the CFHT, which is operated by the National Research Council (NRC) of Canada, the Institut National des Sciences de l'Univers of the Centre National de la Recherche Scientifique (CNRS) of France and the University of Hawaii. This work is based in part on data products produced at TERAPIX and the Canadian Astronomy Data Centre as part of the CFHTLS, a collaborative project of NRC and CNRS. This research uses data from the VIMOS VLT Deep Survey, obtained from the VVDS data base operated by Cesam, Laboratoire d'Astrophysique de Marseille, France. This research has made use of data from the HerMES project (http://hermes.sussex.ac.uk/). HerMES is a Herschel Key Programme utilizing Guaranteed Time from the SPIRE instrument team, ESAC scientists and a mission scientist. The HerMES data were accessed through the *Herschel* Database in Marseille (HeDaM; see http://hedam.lam.fr) operated by CeSAM and hosted by the Laboratoire d'Astrophysique de Marseille.

REFERENCES

Afonso J., Georgakakis A., Almeida C., Hopkins A. M., Cram L. E., Mobasher B., Sullivan M., 2005, ApJ, 624, 135

Afonso J. et al., 2011, ApJ, 743, 122

Appleton P. N. et al., 2004, ApJS, 154, 147

Ballo L., Severgnini P., Della Ceca R., Caccianiga A., Vignali C., Carrera F. J., Corral A., Mateos S., 2014, MNRAS, 444, 2580

Banerji M., Chapman S. C., Smail I., Alaghband-Zadeh S., Swinbank A. M., Dunlop J. S., Ivison R. J., Blain A. W., 2011, MNRAS, 418, 1071

Banfield J. K., George S. J., Taylor A. R., Stil J. M., Kothes R., Scott D., 2011, ApJ, 733, 69

Bardelli S., Zucca E., Bolzonella M., Ciliegi P., Gregorini L., Zamorani G., Bondi M., Parma P., 2009, A&A, 495, 431

Basu A., Wadadekar Y., Beelen A., Singh V., Archana K. N., Sirothia S., Ishwara-Chandra C. H., 2015, ApJ, 803, 51

Bondi M. et al., 2003, A&A, 403, 857

Bondi M. et al., 2007, A&A, 463, 519

Brammer G. B., van Dokkum P. G., Coppi P., 2008, ApJ, 686, 1503

Brookes M. H., Best P. N., Peacock J. A., Röttgering H. J. A., Dunlop J. S., 2008, MNRAS, 385, 1297

Bryant J. J., Johnston H. M., Broderick J. W., Hunstead R. W., De Breuck C., Gaensler B. M., 2009, MNRAS, 395, 1099

Calanog J. A. et al., 2013, ApJ, 775, 61

Chiappetti L., Tajer M., Trinchieri G., Maccagni D., Maraschi L., Paioro L., Pierre M., Arnaboldi M., 2005, A&A, 439, 413

Chuter R. W. et al., 2011, MNRAS, 413, 1678

Ciliegi P., Zamorani G., Bondi M., Pozzetti L., Bolzonella M., Gregorini L., Garilli B., Rizzo D., 2005, A&A, 441, 879

Collier J. D. et al., 2014, MNRAS, 439, 545

Condon J. J., Cotton W. D., Yin Q. F., Shupe D. L., Storrie-Lombardi L. J., Helou G., Soifer B. T., Werner M. W., 2003, AJ, 125, 2411

Dewdney P. E., Hall P. J., Schilizzi R. T., Lazio T. J. L. W., 2009, IEEE Proceedings, 97, 1482

Dunlop J. et al., 2007, Spitzer Proposal, 40021

Fanaroff B. L., Riley J. M., 1974, MNRAS, 167, 31ᴘ

Fanti C., 2009, Astron. Nachr., 330, 120

Furusawa H. et al., 2008, ApJS, 176, 1

Gardner J. P. et al., 2006, Space Sci. Rev., 123, 485

Garn T., Alexander P., 2008, MNRAS, 391, 1000

Geach J. E., Simpson C., Rawlings S., Read A. M., Watson M., 2007, MNRAS, 381, 1369

Ghisellini G., Celotti A., 2001, A&A, 379, L1

Giavalisco M. et al., 2004, ApJ, 600, L93

Herzog A., Middelberg E., Norris R. P., Sharp R., Spitler L. R., Parker Q. A., 2014, A&A, 567, A104

Herzog A., Middelberg E., Norris R. P., Spitler L. R., Deller A. T., Collier J. D., Parker Q. A., 2015a, A&A, 578, A67

Herzog A., Norris R. P., Middelberg E., Spitler L. R., Leipski C., Parker Q. A., 2015b, A&A, 580, A7

Herzog A. et al., 2016, A&A, 593, A130

Higdon J. L. et al., 2005, ApJ, 626, 58

Higdon J. L., Higdon S. J. U., Willner S. P., Brown M. J. I., Stern D., Le Floc'h E., Eisenhardt P., 2008, ApJ, 688, 885

Huynh M. T., Norris R. P., Siana B., Middelberg E., 2010, ApJ, 710, 698

Ilbert O., Arnouts S., McCracken H. J., Bolzonella M., Bertin E., Le Fèvre O., Mellier Y., Vergani D., 2006, A&A, 457, 841

Ishwara-Chandra C. H., Sirothia S. K., Wadadekar Y., Pal S., Windhorst R., 2010, MNRAS, 405, 436

Ivezic Z. et al., 2008, preprint (arXiv:0805.2366)

Ivison R. J. et al., 2007, MNRAS, 380, 199

Jarvis M. J., Rawlings S., Eales S., Blundell K. M., Bunker A. J., Croft S., McLure R. J., Willott C. J., 2001, MNRAS, 326, 1585

Jarvis M. J., Teimourian H., Simpson C., Smith D. J. B., Rawlings S., Bonfield D., 2009, MNRAS, 398, L83

Jarvis M. J., Bonfield D. G., Bruce V. A., Geach J. E., McAlpine K., McLure R. J., Zwart J. T. L., 2013, MNRAS, 428, 1281

Ker L. M., Best P. N., Rigby E. E., Röttgering H. J. A., Gendre M. A., 2012, MNRAS, 420, 2644

Kimball A. E., Ivezić Ž., 2008, AJ, 136, 684

Lacy M., Wilson G., Masci F., Storrie-Lombardi L. J., Appleton P. N., Armus L., Chapman S. C., Yan L., 2005, ApJS, 161, 41

Lawrence A., Warren S. J., Almaini O., Edge A. C., Hambly N. C., Jameson R. F., Lucas P., Folger M., 2007, MNRAS, 379, 1599

Le Fèvre O. et al., 2004, A&A, 417, 839

Le Fèvre O., Cassata P., Cucciati O., Garilli B., Ilbert O., Le Brun V., Zucca E., 2013, A&A, 559, A14

Lonsdale C. J., Smith H. E., Rowan-Robinson M., Surace J., Shupe D., Xu C., Oliver S., Serjeant S., 2003, PASP, 115, 897

Maini A., Prandoni I., Norris R. P., Spitler L. R., Mignano A., Lacy M., Morganti R., 2016, A&A, 596, A80

Mauch T., Sadler E. M., 2007, MNRAS, 375, 931

Mauduit J.-C. et al., 2012, PASP, 124, 714

McAlpine K., Smith D. J. B., Jarvis M. J., Bonfield D. G., Fleuren S., 2012, MNRAS, 423, 132

McAlpine K., Jarvis M. J., Bonfield D. G., 2013, MNRAS, 436, 1084

McCracken H. J. et al., 2003, A&A, 410, 17

Middelberg E., Norris R. P., Tingay S., Mao M. Y., Phillips C. J., Hotan A. W., 2008, A&A, 491, 435

Middelberg E., Norris R. P., Hales C. A., Seymour N., Johnston-Hollitt M., Huynh M. T., Lenc E., Mao M. Y., 2011, A&A, 526, A8

Miley G., De Breuck C., 2008, A&A Rev., 15, 67

Norris R. P. et al., 2006, AJ, 132, 2409

Norris R. P., Tingay S., Phillips C., Middelberg E., Deller A., Appleton P. N., 2007, MNRAS, 378, 1434

Norris R. P. et al., 2011a, PASA, 28, 215

Norris R. P. et al., 2011b, ApJ, 736, 55

Oliver S. J. et al., 2012, MNRAS, 424, 1614

Pentericci L., Van Reeven W., Carilli C. L., Röttgering H. J. A., Miley G. K., 2000, A&AS, 145, 121

Rafter S. E., Crenshaw D. M., Wiita P. J., 2009, AJ, 137, 42

Sanders D. B. et al., 2007, ApJS, 172, 86

Schinnerer E. et al., 2007, ApJS, 172, 46

Seymour N. et al., 2007, ApJS, 171, 353

Simpson C. et al., 2006, MNRAS, 372, 741

Simpson C. et al., 2012, MNRAS, 421, 3060

Singh V. et al., 2014, A&A, 569, A52

Smail I., Sharp R., Swinbank A. M., Akiyama M., Ueda Y., Foucaud S., Almaini O., Croom S., 2008, MNRAS, 389, 407

Tamhane P., Wadadekar Y., Basu A., Singh V., Ishwara-Chandra C. H., Beelen A., Sirothia S., 2015, MNRAS, 453, 2438

Tinti S., de Zotti G., 2006, A&A, 445, 889

Ueda Y. et al., 2008, ApJS, 179, 124

van Breukelen C. et al., 2009, MNRAS, 395, 11

Willott C. J., Rawlings S., Jarvis M. J., Blundell K. M., 2003, MNRAS, 339, 173

Wright E. L. et al., 2010, AJ, 140, 1868

Zinn P.-C., Middelberg E., Ibar E., 2011, A&A, 531, A14

APPENDIX A: IFRS IMAGES
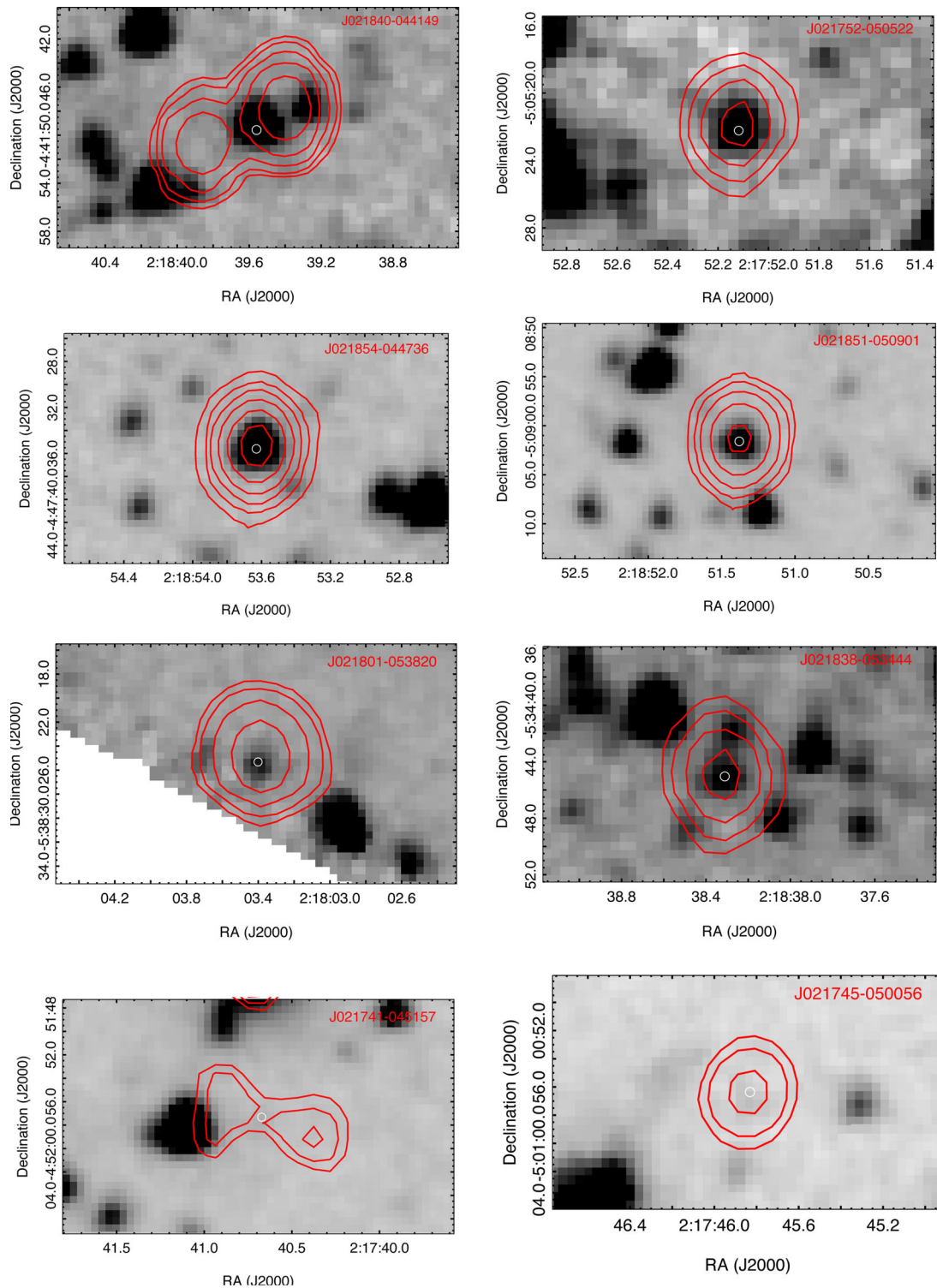
Figure A1. 1.4-GHz radio contours of our IFRSs overplotted on to 3.6-μm grey-scale images. The outermost first radio contour begins at 5σ with successive contour levels increased by a factor of √2. White circles represent the radio positions of the IFRSs.
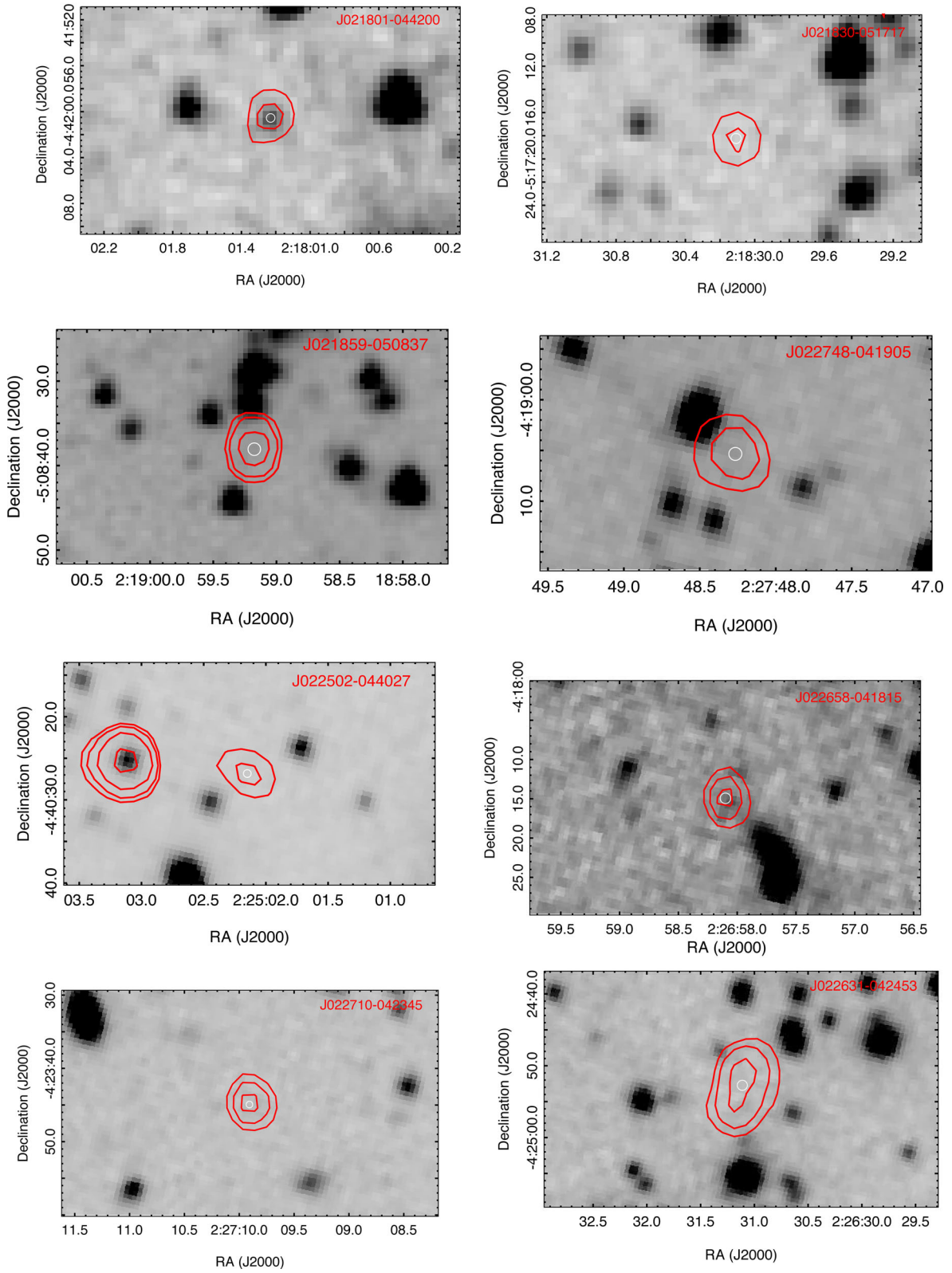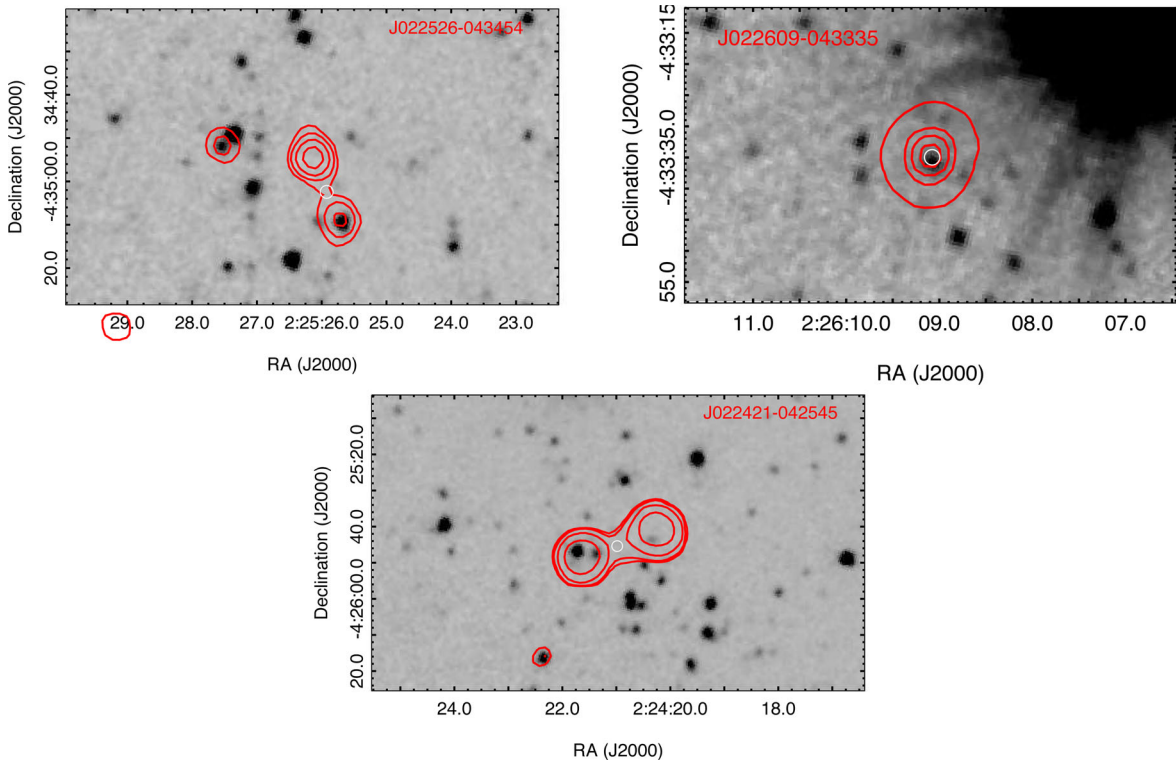
Figure A1 – *continued*

Figure A1 – *continued*

This paper has been typeset from a TEX/LATEX file prepared by the author.